universität wien

MASTERARBEIT / MASTER'S THESIS

Titel der Masterarbeit / Title of the Master's Thesis

„Non-local interference via path-entanglement over a 411m long multicore fibre“

verfasst von / submitted by

Michael Bartokos, BSc BSc

angestrebter akademischer Grad / in partial fulfilment of the requirements for the degree of

Master of Science (MSc)

Wien, 2022 / Vienna, 2022

Studienkennzahl lt. Studienblatt / degree programme code as it appears on the student record sheet:	UA 066 876
Studienrichtung lt. Studienblatt / degree programme as it appears on the student record sheet:	Physik UG2002
Betreut von / Supervisor:	Mag. Dr. Marcus Huber

Abstract

In this proof-of-principle experiment path-entanglement was verified by non-locally interfering two neighbouring core pairs of a multi-core fibre (MCF). The entangled photons are generated inside a non-linear crystal and simulations show the rotationally symmetric distribution and temperature dependent spectral characteristics. They are then mapped onto the end-face of the MCF, which is used to guide the photons to two distinct interferometers, where the photons interfere on a beamsplitter and coincidences are measured. Even though the setup was not stabilized, it reaches visibilities up to 97 %, making this technique suitable for quantum key generation and distribution applications. This experiment shows that a MCF is suitable for entanglement distribution and the wavelength of the photons (1560 nm) makes this technique integrable for existing telecommunication infrastructure.

Zusammenfassung

In diesem Grundsatzbeweis wird Pfadverschränkung über nicht-lokale Interferenz zweier benachbarten Paaren einer mehrkernigen Faser nachgewiesen. Die Photonen werden in einem nicht-linearem Kristall erzeugt und Simulationen zeigen die rotationssymmetrische Verteilung und temperaturabhängigen Eigenschaften. Diese werden anschließend auf die Faser projiziert, welche verwendet wird um die Photonon zu zwei verschiedenen Interferometern zu leiten, wo sie an einem Strahlenteiler interferieren und Koinzidenzen gemessen werden. Obwohl der Aufbau dieses Experiments nicht stabilisiert wird, werden Sichtbarkeiten von über 97 % erreicht, weshalb sich diese Technik für Quantenschlüssel-Generations- und Verteilungs-Anwendungen eignet. Dieses Experiment zeigt, dass eine mehrkernige Faser Verschränkungsverteilung und die verwendete Wellenlänge (1560 nm) die Integration in bestehende Telekommunikationsinfrastruktur ermöglicht.

Table of Contents

1 Introduction

Asymmetrical or *public-key cryptosystems* like for example *RSA* [1] are the most widely used systems for en- and decryption. It uses different keys for both and its security relies on computational complexity with the idea of *one-way functions* - functions that are easy to compute in one direction, but the task of solving them the other way round grows exponentially with each new input bit. In fact, even though this makes cryptosystems very secure, at the same time it's its weakness. Assumptions made for their security are unproven (or even unprovable) and therefore it cannot be excluded that someday an algorithm is good enough to execute those tasks way faster than initially thought. Hence, a new way of secure communication has to be established. Especially with quantum computers on the way which exploit phenomenons like superposition and entanglement to increase computational power by magnitudes.
Quantum cryptography is said to be the most secure way for information encryption. It uses only a single key for both, en- and decryption and falls under the definition of *symmetrical* or *secure-key* cryptosystems. To share encrypted information supported by quantum objects, e.g. photons, the field of quantum key distribution (QKD) deals with the possibilities of how to do so – meaning how to share the (quantum) key which en- and decrypts the secret message. The superior advantage of quantum instead of classical keys is the usage of the so-called *no-cloning theorem* [2] which states that no quantum state can be copied without altering its initial state - it perturbates this system. Several protocols have already been proposed and verified how such security checks would look like, for example the famous *BB84 protocol*, developed by C. Bennett and G. Brassard in 1984 [3]. As soon as both parties know that the key was not intercepted by an eavesdropper they can exchange encrypted messages through classical channels because nobody except the trusted nodes has the key to begin with. QKD is hard to establish due to the high sensitivity of quantum systems, which are easily prone to errors. But several methods, settings and quantum error-correction algorithms have already been developed, leading to many breakthroughs - e.g. [4–10]. Distribution of a secure key can happen via satellites, free-space links or through optical fibres. While single mode fibres (SMF) are already in various applications, there are also multicore fibres (MCF) used - a single fibre with several cores facilitating infrastructure by enhancing the capacity of information distribution.

The aim of this thesis is a proof-of-principle experiment to verify non-local interference via path-entanglement that is shown by exploiting the spatial correlations between an entangled photon pair created in a type-0 SPDC source and using a MCF for guiding those. This technique can be used for example for the generation and subsequent distribution of the key to one or even several parties and can easily be implemented into already existing telecommunication infrastructure.
In chapter 2 basic ideas are presented such as entanglement, the Mach-Zehnder interferometer and path-entanglement itself. Chapter 3 deals with the setup - from the source to the detector - as well as the alignment and measurement procedures and a short comment on the stability. In the end, chapter 4 presents the results and analysis of the data by computing visibilites.

2 Basic ideas

In this chapter we will discuss what entanglement is, how it can be created and dive into the basic idea behind the experiment exploiting this phenomenon.

2.1 Entanglement

> *The phenomenon of entanglement is the essential fact of quantum mechanics, the fact that makes it so different from classical physics. It brings into question our entire understanding about what is real in the physical world.*
>
> -Leonard Susskind [11]

Entanglement is an intrinsic quantum mechanical feature defying classical physics as nothing else does. It led to Einstein talking about "spooky action at a distant" due to the seemingly superluminous communication between two quantum systems. Nowadays, entanglement can be and is used in a variety of disciplines, for example in foundational physics, in biochemical processes [12, 13] and it is currently starting to get into focus of medical research [14], while being a fundamental property for quantum computation and communication. By exploiting the fact that using a third quantum system one can swap the entanglement between different parties, it has already been shown that one can "teleport" information further than 1000 km, see for example [15–18]. *Entanglement swapping* is also used to improve the fidelity of the entanglement, since the quality of entanglement gets reduced after a certain time and distance. This procedure is called *entanglement distillation* or *purification* [19–21].

2.1.1 Definition

Consider a composite quantum system consisting of two pure states labeled a and b. The composite state can then be written as a product state

$$|\psi\rangle = |\phi\rangle_a \otimes |\theta\rangle_b = |\phi\rangle_a |\theta\rangle_b = |\phi\,\theta\rangle_{ab} = |\phi\,\theta\rangle \tag{1}$$

Now if there is a state that cannot be written in such a product state, meaning each system cannot be described on its own, then it is called an entangled state. Using the density matrix

$$\hat{\rho}_{ab} = |\phi\rangle\langle\phi| \otimes |\theta\rangle\langle\theta| \tag{2}$$

one can establish the reduced density operator for a subsystem by taking the trace over the other:

$$\hat{\rho}_a = |\phi\rangle\langle\phi| \tag{3}$$

For any non-entangled pure state it holds that

$$\mathrm{Tr}(\hat{\rho}_a^2) = 1 \tag{4}$$

while this condition is not fulfilled for entangled states:

$$\mathrm{Tr}(\hat{\rho}_a^2) \neq 1 \tag{5}$$

These separability conditions hold for pure states. A general (mixed) state is known to be separable if the state can be expressed as the sum of separable pure states, weighted by a probability factor p_i (where $\sum_i p_i = 1$)[22]:

$$\rho_{\mathrm{sep}} = \sum_i p_i |\phi_i\rangle\langle\phi_i| \otimes |\theta_i\rangle\langle\theta_i| \tag{6}$$

It is not always possible to determine the state itself to confirm entanglement, but rather use different notions such as the *positive partial transpose* (PPT) [23, 24] or *entanglement witness* [25]. For a review about entanglement certification, see for example [26].
There is particularly a set of states that are very prominent, namely the *Bell states* which are maximally entangled:

$$|\Psi^-\rangle = \frac{1}{\sqrt{2}}(|01\rangle - |10\rangle)$$
$$|\Psi^+\rangle = \frac{1}{\sqrt{2}}(|01\rangle + |10\rangle)$$
$$|\Phi^-\rangle = \frac{1}{\sqrt{2}}(|00\rangle - |11\rangle)$$
$$|\Phi^+\rangle = \frac{1}{\sqrt{2}}(|00\rangle + |11\rangle)$$

$|0\rangle$ and $|1\rangle$ are just the states of a two-level system in the computational basis. The first one is also called a singlet state (and is anti-symmetric under interchange of the qubits[1]). Those can be used to violate the Bell inequality which led to discarding the hidden variable theories [27–29]. One can clearly see that measuring one state instantaneously determines the state of the second qubit.

2.1.2 Degrees of freedom

Quantum entanglement describes the fact that one or more properties of two different systems correlate with each other in two non-commuting bases - so there exist different types of entanglement. For example, inside a BBO (Barium Borate) crystal one can produce polarization entangled photons via down conversion (see next section) in which case the Bell states look as follows:

$$\begin{aligned} |\Psi^-\rangle &= \frac{1}{\sqrt{2}}(|HV\rangle - |VH\rangle) & |\Phi^-\rangle &= \frac{1}{\sqrt{2}}(|HH\rangle - |VV\rangle) \\ |\Psi^+\rangle &= \frac{1}{\sqrt{2}}(|HV\rangle + |VH\rangle) & |\Phi^+\rangle &= \frac{1}{\sqrt{2}}(|HH\rangle + |VV\rangle) \end{aligned} \tag{7}$$

with $|H\rangle$ and $|V\rangle$ being horizontal and vertical polarization, respectively. Then there is time-energy entanglement or frequency bin entanglement that is also given by the down conversion process [30, 31]. The important type for this thesis is path-entanglement, meaning there is a correlation of the number of photons in different paths which can lead to non-local interference. Prominent in quantum information are the so called multiphoton entangled *NOON-states*:

$$|\Psi\rangle_{\text{NOON}} = \frac{1}{\sqrt{2}}\left(|N,0\rangle + e^{iN\phi}|0,N\rangle\right) \tag{8}$$

where N is the number of photons in its respective path and the exponent just a phase factor [32–34]. This type of entanglement will be described in more detail in section 2.3.
Now, entangled systems do not have to be entangled in just one degree of freedom (doF) but they can exist in more than one. This phenomenon is called *hyperentanglement* and promises further possibilities of information processing [35–37].

[1] Short for quantum bit.

2.1.3 Generation

Since its first demonstration in 1970 [38] *spontaneous parametric down conversion* (SPDC) has become one of the most widely used techniques for the creation of entangled photon pairs. It uses the non-linearity of the polarization in a medium to annihilate one pump-photon and re-emit two photons with twice its wavelength which are then entangled.
A dielectric medium response to an external applied electric field via the polarization:

$$\vec{P} = \varepsilon_0 \chi^{(1)} \vec{E} + \varepsilon_0 \chi^{(2)} \vec{E}^2 + \mathcal{O}(\vec{E}^3) \tag{9}$$

where ε_0 is the vacuum permittivity, χ the electric susceptibility of the medium and $\vec{E}$ the electric field itself. While free space propagation stays linear, in some media the non-linear terms cannot be neglected. For SPDC it is sufficient to approximate the polarization to second order and discard higher order terms. SPDC is a three-wave mixing effect (also known as *parametric interaction*) in which a pump photon with frequency ω_p is down converted into two photons which are usually called *signal* (with frequency ω_s) and *idler* (with frequency ω_i). While the photon number is not, energy is conserved:

$$\omega_p - \omega_s - \omega_i = 0 \tag{10}$$

The same holds for the momentum:

$$\vec{k}_p - \vec{k}_s - \vec{k}_i = 0 \tag{11}$$

where the wave vectors $\vec{k}_j$ with $j = p, s, i$ are defined as:

$$|\vec{k}_j| = \frac{n_j(\omega_j) \cdot \omega_j}{c} = \frac{2\pi \cdot n_j(\omega_j)}{\lambda} \tag{12}$$

Here $n_j(\omega_j)$ is the frequency dependent refractive index that leads to chromatic dispersion and c the speed of light. The relation between the refractive index of a medium and the wavelength λ is given by the *Sellmeier equation*:

$$n^2(\lambda) = a_1 + b_1 f + \frac{a_2 + b_2 f}{\lambda^2 - (a_3 + b_3 f)^2} + \frac{a_4 + b_4 f}{\lambda^2 - a_5^2} - a_6 \lambda^2 \tag{13}$$

Here, f is a temperature dependent parameter and the a_i and b_j ($i = 1, ..., 6$ and $j = 1, ..., 4$) are coefficients - details can be found in, e.g. [39]. For crystals in which all three fields propagate collinearly, the relation

$$\frac{\vec{k}_p}{|\vec{k}_p|} = \frac{\vec{k}_s}{|\vec{k}_s|} = \frac{\vec{k}_i}{|\vec{k}_i|} \tag{14}$$

holds and Eq. (11) can be written as a scalar expression:

$$\frac{n_p(\omega_p)}{c} \cdot \omega_p - \frac{n_s(\omega_s)}{c} \cdot \omega_s - \frac{n_i(\omega_i)}{c} \cdot \omega_i = 0 \tag{15}$$

Eq. (15) is called *phase-matching condition*. If this condition is not fulfilled a phase mismatch and destructive interference (after a certain distance) occurs due to a resulting difference of the propagation speed of each field inside the crystal. One solution to this problem

is to engineer the crystal itself in a way that the phases match again. This is known as *quasi phase-matching* (QPM) [40–42] with the QPM condition:

$$\Delta\vec{k} = \vec{k}_p - \vec{k}_s - \vec{k}_i - \vec{k}_m \tag{16}$$

The grating wave vector $\vec{k}_m$ is defined as $|\vec{k}_m| = 2\pi/\Lambda$ with the poling period length Λ of the crystal. If the photon is propagating along a principal axis, e.g. the z-axis, Eq. (16) can be rewritten, using the transverse wave vectors $\vec{q}_j$ $(j = s, i)$ and Eq. (12):

$$\Delta k^z = 2\pi \left(\frac{n_p}{\lambda_p} - \frac{n_s}{\lambda_s} - \frac{n_i}{\lambda_i} - \frac{1}{\Lambda} \right) + \frac{|\vec{q}_s - \vec{q}_i|^2}{2k_p^z} \tag{17}$$

The spatial distribution of the emitted photons can then be computed by squaring the *bi-photon mode function* $\Phi(\vec{q}_s, \vec{q}_i)$ [43, 44]:

$$\Phi(\vec{q}_s, \vec{q}_i) \sim e^{-\frac{|\vec{q}_s + \vec{q}_i|^2 \omega_p^2}{4}} \operatorname{sinc}\left(\frac{L}{2} \cdot \Delta k^z \right) \tag{18}$$

where ω_p is the angular frequency of the pump photon and L the length of the crystal. A crystal that uses QPM emits the photons in one cone, where the entangled photons are on opposite ends (Fig. 1). By using the fact that the emission is rotationally symmetric one can define the emission angle relative to the principle axis of the crystal with the x-component of the transverse wave vector $\vec{q}_j$ $(j = s, i)$:

$$\theta_j = \arctan \frac{|q_j^x|}{|k_j^z|} \tag{19}$$

where the z-component points in the direction of the pump beam. This angle corresponds to the propagation inside the crystal. The emission-angle after the transition from crystal to air is given by *Snell's law*:

$$n_C \sin\theta_C = n_A \sin\theta_A \tag{20}$$

Here, n_C and θ_C are the refractive index and incident angle inside the crystal, while $n_A = 1$ and θ_A account for the air side. By changing the temperature and therefore changing the phase matching condition, Eq. (15), of the crystal one can tweak the wave vectors and frequencies of the entangled photon pair (see section 3.1.1). Even though SPDC is a widely used technique for entanglement creation it is also very inefficient because $\chi^{(2)}$ is still very small. The conversion happens via random vacuum fluctuations which is a very rare event - for example only one in 10^{12} photons gets down converted [45].
There are three different types of SPDC processes that define the polarization of the signal and idler photons:

- Type 0: The polarization of signal and idler is parallel to the polarization of the pump photon
- Type 1: The polarization of signal and idler is orthogonal to the polarization of the pump photon
- Type 2: The polarization of signal and idler is orthogonal with respect to each other, where by convention the signal photon's polarization is parallel to the polarization of the pump photon[2]

[2]This is only true in the degenerate case, in the non-degenerate regime the photon with higher frequency is referred to as signal photon.

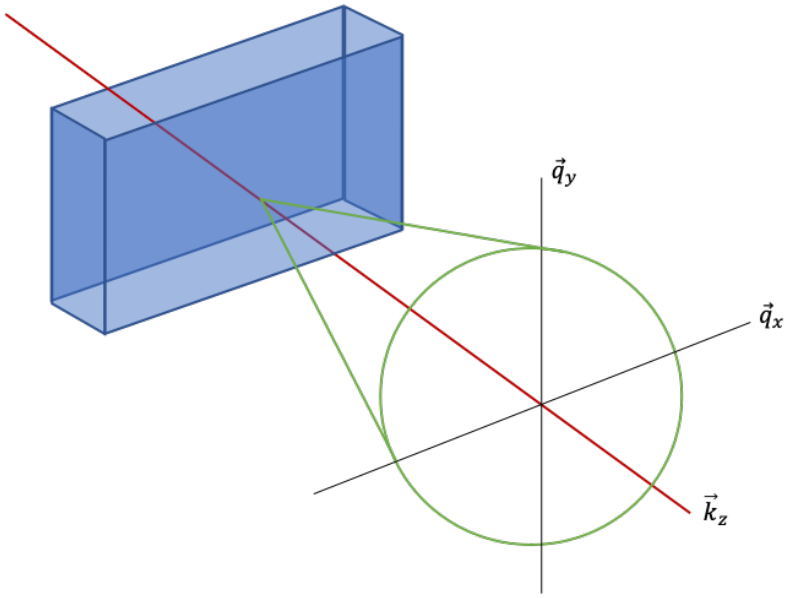

Fig. 1: Emssion cone of a type-0 SPDC source. The pump photons (red) propagate along the z-axis and enter the crystal (blue), which annihilates the photon emitting two entangled photons which lie diametrically symmetric on the cone's surface (green).

2.2 Mach-Zehnder Interferometer

The Mach-Zehnder (MZ) interferometer consists of two beamsplitters (BS) and a phase-shifter (PS) in one arm (see Fig. 2). A BS acts as a unitary transformation with the unitary matrix[3]:

$$\hat{U}_{\mathrm{BS}} = \frac{1}{\sqrt{2}} \begin{pmatrix} 1 & i \\ i & 1 \end{pmatrix} \tag{21}$$

where the i comes from the $\pi/2$ phase shift in the reflection mode due to the unitarity of operation [46] and the PS unitary operator:

$$\hat{U}_{\mathrm{PS}} = \begin{pmatrix} e^{i\phi} & 0 \\ 0 & 1 \end{pmatrix} \tag{22}$$

After the second BS a detector is placed at each output mode and clicks when detecting a photon. The detection probability for detector 1 and detector 2 are given by:

$$\begin{aligned} p_1 &= \cos^2 \frac{\phi}{2} \\ p_2 &= \sin^2 \frac{\phi}{2} \end{aligned} \tag{23}$$

respectively, leading to interference fringes as can be seen in Fig. 3. In other words a photon is in a superposition of being in one or the other arm after the first BS and overlaps with itself at the second BS. Depending on the phase constructive or destructive interference occurs towards one of the outputs, so only one detector sees the photon. Hence, changing the length of one arm (physically or by placing a PS in the photon's path) leads to interference fringes at the output and one can control where the photon lands.

[3] Here we assume a 50/50 beamsplitter, meaning that it transmits and reflects the photons with equal probability.

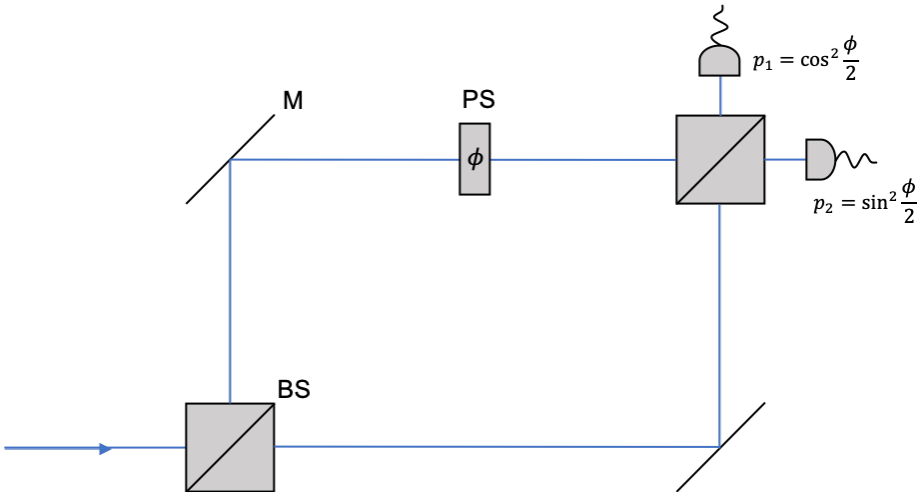

Fig. 2: A Mach-Zehnder interferometer consisting of two beamsplitters (BS) and a phase-shifter (PS), with M being a mirror. The path-superposition after the first BS leads to interference fringes at the detectors.

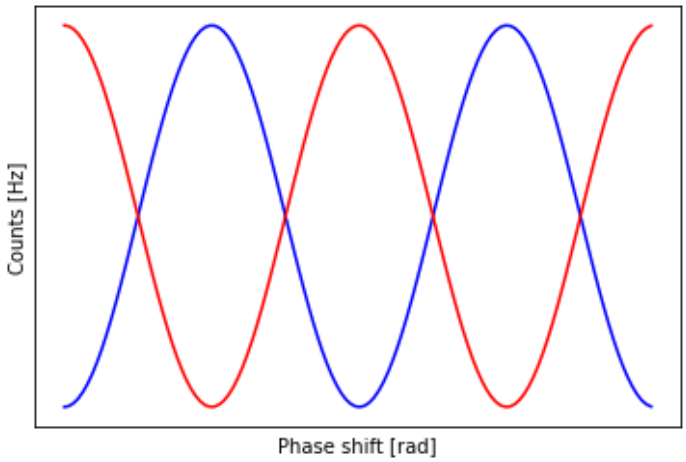

Fig. 3: Interference fringes as predicted by Eq. (23).

A quality measure for interference is the so-called *visibility* which basically is a contrast between the maximum and minimum of the curves (counts) in Eq. (23) and shows how good the interference is. It is defined as the ratio between the difference over the sum of the maximum and minimum counts C:

$$V = \frac{C_{\max} - C_{\min}}{C_{\max} + C_{\min}} \tag{24}$$

2.3 Path entanglement and non-local interference

Fig. 4 shows the idea behind the experiment. One photon of an entangled pair is in a superposition of taking the path $|A_1\rangle$ and $|A_2\rangle$ (so being in two interferometers simultaneously), while the same holds for the other partner for $|B_1\rangle$ and $|B_2\rangle$. At the beamsplitter the entangled photons will be in a state $|A_1A_2\rangle$ or $|B_1B_2\rangle$, depending on the path they took (the experimental reason for that will be explained in section 3.1.3). Therefore, two photons are in a superposition of being in all four arms of two interferometers and can therefore interfere

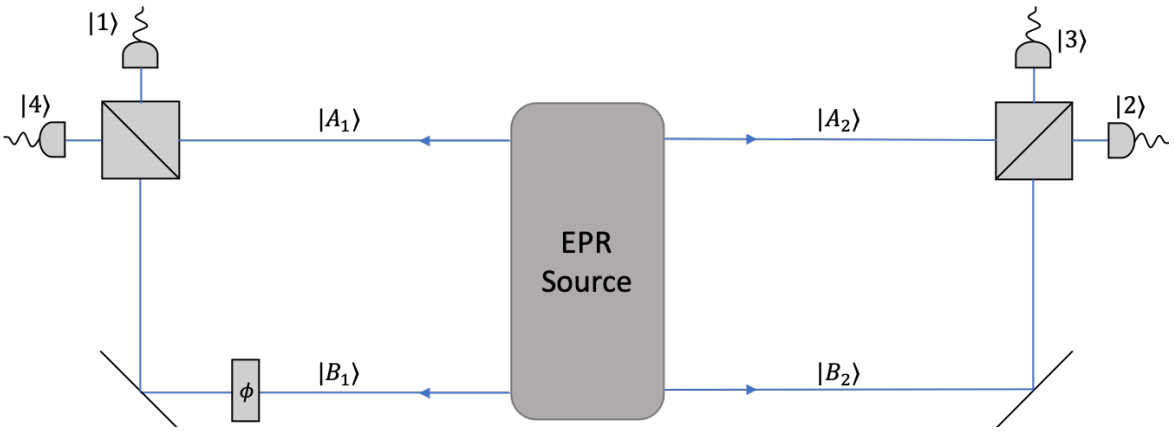

Fig. 4: Each photon of an entangled pair created in the EPR Source is in a superposition of taking the paths $|A_1\rangle$ and $|A_2\rangle$ as well as $|B_1\rangle$ and $|B_2\rangle$ for the other photon. Detectors are labeled as they were named in the experiment itself. At the BS they overlap, leading to non-local interference.

with each other at both BS. The input state before the BS looks as following:

$$|\Psi_{\text{in}}\rangle = \frac{1}{\sqrt{2}}\left(|A_1A_2\rangle - e^{i\phi}\,|B_1B_2\rangle\right) \tag{25}$$

The beamsplitter now acts on each photon as a unitary transformation as given by Eq. (21) and we label each output the same as it was named in the actual experiment:

$$|A_1\rangle \to \frac{1}{\sqrt{2}}\left(|4\rangle + i\,|1\rangle\right) \qquad |B_1\rangle \to \frac{1}{\sqrt{2}}\left(|1\rangle + i\,|4\rangle\right)$$
$$|A_2\rangle \to \frac{1}{\sqrt{2}}\left(|2\rangle + i\,|3\rangle\right) \qquad |B_2\rangle \to \frac{1}{\sqrt{2}}\left(|3\rangle + i\,|2\rangle\right)$$

We can plug that into the input in Eq. (25) to get the output state:

$$\begin{aligned}|\Psi_{\text{out}}\rangle &= \frac{1}{2\sqrt{2}}\left[\left(|4\rangle + i\,|1\rangle\right)\left(|2\rangle + i\,|3\rangle\right) - e^{i\phi}\left(|1\rangle + i\,|4\rangle\right)\left(|3\rangle + i\,|2\rangle\right)\right] = \\ &= \frac{1}{2\sqrt{2}}\left(|42\rangle + i\,|43\rangle + i\,|12\rangle - |13\rangle - e^{i\phi}\,|13\rangle - ie^{i\phi}\,|12\rangle - ie^{i\phi}\,|43\rangle + e^{i\phi}\,|42\rangle\right)\end{aligned}$$

Using the fact that $|\text{jk}\rangle = |\text{kj}\rangle$ with $\text{j} \neq \text{k}$ the expression can be simplified as:

$$|\Psi_{\text{out}}\rangle = \frac{1}{2\sqrt{2}}\left[\left(1 + e^{i\phi}\right)|24\rangle + \left(i - ie^{i\phi}\right)|34\rangle + \left(i - ie^{i\phi}\right)|12\rangle - \left(1 + e^{i\phi}\right)|13\rangle\right] \tag{26}$$

This can now be summarized as:

$$|\Psi_{\text{out}}\rangle = \frac{1}{2\sqrt{2}}\left[\left(1 + e^{i\phi}\right)\left(|24\rangle - |13\rangle\right) + \left(i - ie^{i\phi}\right)\left(|12\rangle + |34\rangle\right)\right] \tag{27}$$

The magnitude squared of the coefficients from each term gives the probability of coincidences of the respective detector-pair, meaning a simultaneous measurement (or 'click') in both detectors. Those probabilities can be rewritten by using the following relations:

$$\cos^2 x = \frac{1 + \cos 2x}{2} \qquad \sin^2 x = \frac{1 - \cos 2x}{2}$$

which lead to a more familiar pattern:

$$\begin{aligned} |34\rangle &\propto \sin^2\frac{\phi}{2} \qquad |24\rangle \propto \cos^2\frac{\phi}{2} \\ |12\rangle &\propto \sin^2\frac{\phi}{2} \qquad |13\rangle \propto \cos^2\frac{\phi}{2} \end{aligned} \tag{28}$$

These probabilities show that by changing the relative phase in one arm the coincidence rate in almost all detector pairs correlate with and influence each other and we observe non-local interference. The only two detectors that don't show coincidences are $|14\rangle$ and $|23\rangle$, since - as with the Mach-Zehnder interferometer - the photons exit only at one output at the BS. From this one expects interference fringes that look the same as in Fig. 3 but with the blue function being the coincidence counts for $|12\rangle$ & $|34\rangle$ and red for $|13\rangle$ & $|24\rangle$.

3 Experiment

3.1 Setup

The setup can be divided in four components: 1) the SPDC source for generating the entangled photons, 2) the multicore fibre guiding the photons to 3) the interferometers and 4) the detector. We will discuss the characteristics of each building block in detail.

3.1.1 SPDC source

This source was used and spectrally analyzed before by [44] with a different poling period. The entangled photons are produced during a type-0 SPDC process in a magnesium-oxid-doped periodically poled lithium niobate (MgO:ppLN) crystal of length $L = 40\,\text{mm}$ and a poling period of $\Lambda = 19.5\,\mu\text{m}$. As already discussed above, spectral characteristics and emission angle of the signal and idler photons can be varied by modifying the crystal's temperature. Computing the squared bi-photon function in Eq. (18) under the assumption of rotational symmetry and the fact that signal and idler have opposite transverse wavevectors ($\vec{q}_s = -\vec{q}_i$), gives the spatial distribution of both photons for a specific temperature that can be seen in Fig. 5. The temperature dependent emission angle of the photons can be simulated by searching for the minimum of Eq. (17) and calculating the magnitude of the transverse wave vector. q can then be used in Eq. (19) for the emission angle. Snell's law (Eq. (20) can then be used to get the angle after exiting the crystal. This simulation is illustrated in Fig. 6 (left). Neglecting the last term in Eq. (17) and minimizing again for λ_s and λ_i results in the temperature dependent center wavelength of the signal and idler photons. This bifurcation behaviour is depicted in Fig. 6 (right). The spatial distribution of the photons (Fig. 5) gives a ring-like structure, which is then used to cover all cores of the multicore fibre in either the inner or outer ring (see next section). With increasing temperature the emission angle is reduced, until it reaches a collinear output at about 78°C (Fig. 6 (left)). The center wavelengths of the entangled pair reaches non-degeneracy at ~ 78°C, below they are degenerate (Fig. 6 (right)).
In this experiment, the crystal is pumped with photons with a wavelength of $\lambda_p \sim 780\,\text{nm}$, producing entangled photons at telecommunication wavelength of $\lambda_s = \lambda_i = 1560\,\text{nm}$. The crystal's temperature is set at $T = 77.50$°C, while it actually regulates slightly above at $T = 77.53(9)$°C due to imperfections. The whole source looks as depicted in Fig. 7: The 780 nm pump photons from the continuous wave (CW) laser pass a polarizing beam splitter (PBS) and are rotated into the diagonal basis at the adjacent half-wave plate (HWP) which changes the power splitting at the Sagnac-loop. The yttrium orthovanadate plate (YVO_4) retards the photons (vertically polarized photons are slowed down). The crystal itself is placed inside of a Sagnac-loop or Sagnac-configuration [48], which comes from the same-named interferometer. In such a configuration a entangled photon pairs is produced by placing a PBS at the beginning of the loop, such that the crystal gets pumped from one of both sides. Hence, an entangled pair propagates back to the PBS. The SPDC process only works for vertically polarized photons, so a HWP is placed in the arm where horizontally polarized photons are transmitted. Therefore, we get a $|\Phi^+\rangle$ state as in Eq. (7). A dichroic mirror (DM) that transmits the pump photon and reflects the entangled photons, lead them subsequently through a spatial correlation adjustment configuration (Fig. 8) - consisting of lenses and filters - to a multicore fibre (MCF). For more information on the lens setup see [49].

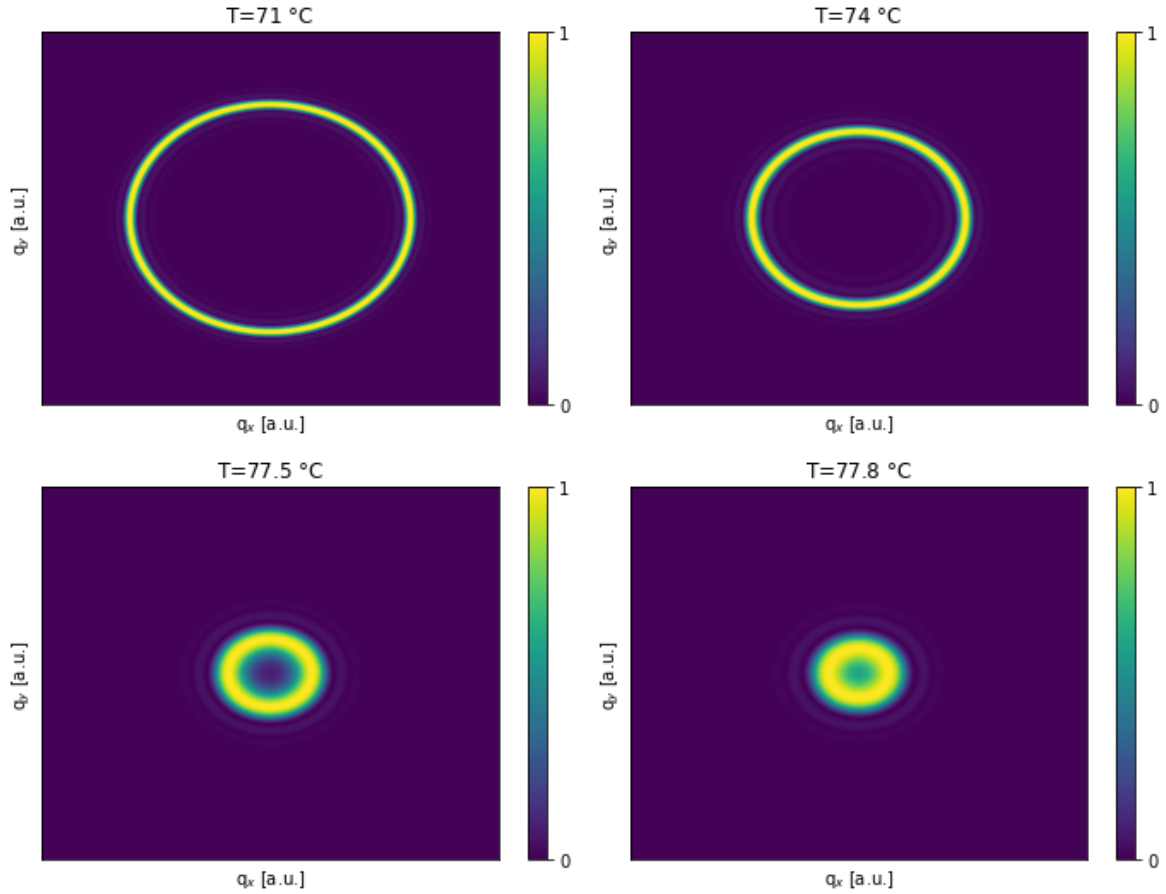

Fig. 5: Simulated spatial intensity distribution of the entangled pair at the far-field plane in terms of the transverse wave vectors with $\lambda_s = \lambda_i = 1560\,\text{nm}$ for a crystal temperature of $T = 71, 74, 77.5$ and $77.8°\text{C}$.

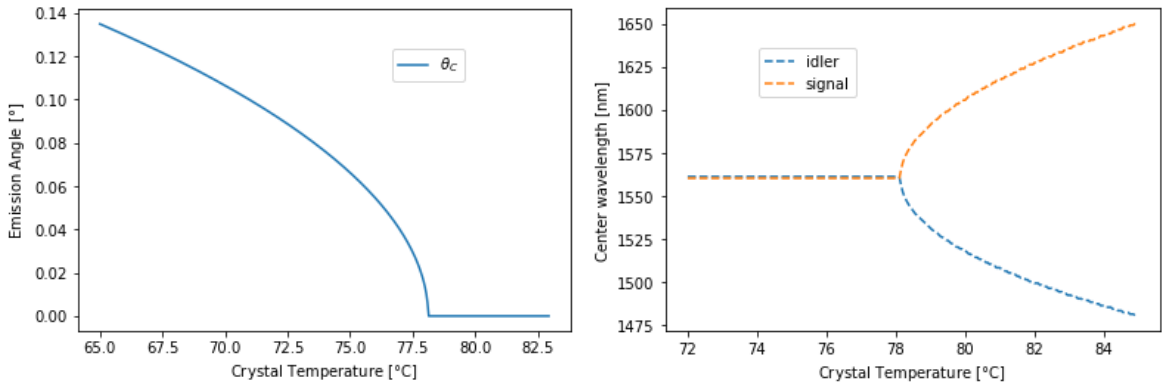

Fig. 6: (Left) Emission angle of the entangled photons after generation inside the crystal for a wavelength of $\lambda_s = \lambda_i = 1560\,\text{nm}$. (Right) Center wavelength of the entangled photons. Beneath around 78°C they reach degeneracy. Both plots are depicted in dependency of the crystal's temperature.

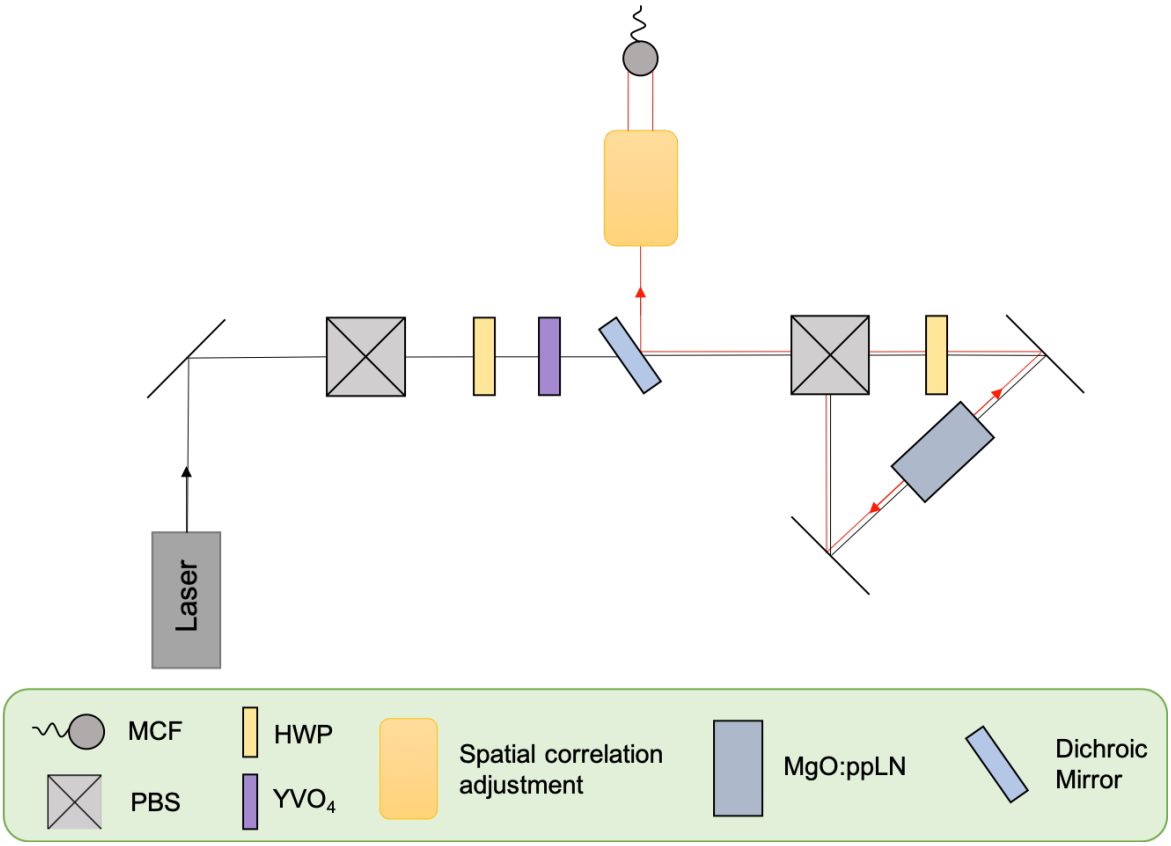

Fig. 7: Schematic of the source. A continuous wave (CW) laser at 780 nm (black line) pumps a MgO:ppLN crystal inside of a Sagnac-loop which produces polarization entangled photon pairs of 1560 nm via SPDC (red line). The spatial correlation adjustment system consists of three lenses, a long-pass and a band-pass interference filter which map the photons onto the MCF. Its principal concept is illustrated in Fig. 8. MCF: Multicore fibre, PBS: polarization beamsplitter, HWP: half-wave plate, YVO4: yttrium orthovanadate plate

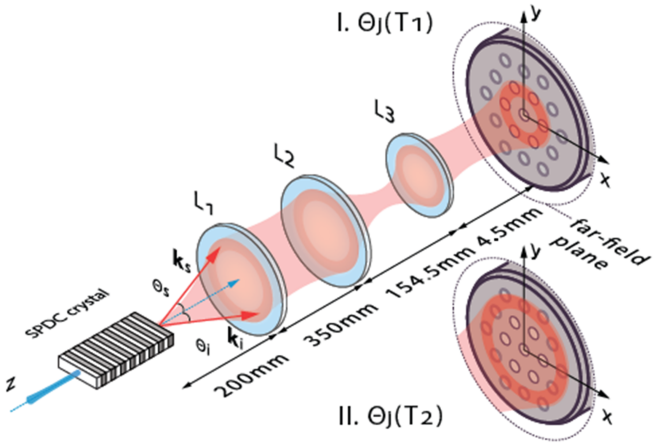

Fig. 8: Sketch of the working principal of the spatial correlation adjustment system that demagnifies the far-field plane onto the MCF's end-face (see next section). The size of the cone of the photons (or the angle) can be modified by changing the crystal's temperature, mapping them onto the inner or outer ring. Image taken from [47].

3.1.2 Multicore fibre

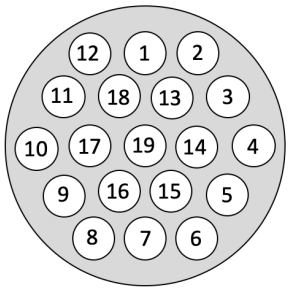

Fig. 9: Structure of the 19-core multicore fibre.

For the distribution of quantum information, optical fibres offer a simple option as a quantum channel besides free-space links [4, 50] and satellites [51] as they are already exhaustively in use. Further development to increase the capacity of those quantum channels, for example via multiplexing [52] is therefore of high interest. Different doF have already been exploited to implement such multiplexing methods [53–55] while the spatial modes of light have been demonstrated to be of good use more recently [49]. Space-division multiplexing (SDM) is currently under investigation, not only for quantum communication schemes but also in classical communication [56]. For SDM to work, a multicore fibre was used (where each core of the MCF is an individual single-mode fibre) since it offers distinguishability of discrete propagation paths. Another reason is to avoid mode-coupling effects [57] and having a higher stability [58] with a much simpler implementation as for multi- or few-mode fibres [59]. MCFs enable the use of high-dimensional quantum communication [60, 61] as well as the transmission [62] and generation [63] of entangled states. The MCF used in [49] is the same that we used for this experiment.

As mentioned before, the wave vectors of signal and idler have opposite transverse components and by looking at the far-field plane[4] of the crystal the photons are at diametrically opposite points. The spatial correlation adjustment system in Fig. 8 then maps the far-field plane onto the MCF's end-face. This means that entangled photons propogate to directly opposite cores of the MCF.

The 411 m long MCF was fabricated at CREOL in the University of Central Florida for the fundamental mode at 1550 nm. The 19 cores (each having a diameter of $\sim 8.5\,\mu$m) are placed hexagonally symmetric with a distance of $\sim 32.25\,\mu$m to each other (see Fig. 9). A central core is surrounded by two hexagonal rings of cores, with the inner ring consisting of 6 cores and the outer ring having 12 cores. A fan-in/fan-out (FIFO) device connects each core to a single-mode fibre (SMF). The symmetrical intensity distribution of the entangled photons (Fig. 5) allows to illuminate each ring fully by changing the temperature of the crystal, where in this experiment a temperature of $T = 77.50°$C corresponds to the outer ring.

Measuring the coincidences for each core (path) showed low cross-correlations between cores as was expected since entangled pairs propagate through opposite paths. For quantification reasons [49] introduced a quasi-*path visibility*[5] defined as:

$$V_{\text{path}}(m) = \frac{C_{mm'} - \frac{\sum_{l\neq m,m'} C_{ml}}{N}}{C_{mm'} + \frac{\sum_{l\neq m,m'} C_{ml}}{N}} \tag{29}$$

where $V_{\text{path}}(m)$ describes the path visibility for core m, $C_{mm'}$ is the coincidence rate between the opposite cores m and m' and the sum over C_{ml} with $l \neq m, m'$ are the cross-correlations or coincidences between non-opposite paths in the same ring. N is the number of non-opposite combinations which are used to weight the sum to "*assure a balanced consideration of wanted (opposite) and unwanted (non-opposite) correlations*" [49]. The authors claimed a

[4] In the far-field the momentum of the photons gets mapped onto the MCF, while in the near-field the position space is the relevant one.

[5] This is not a visibility in the usual way, but rather a measure of how good cross-correlations are not occurring.

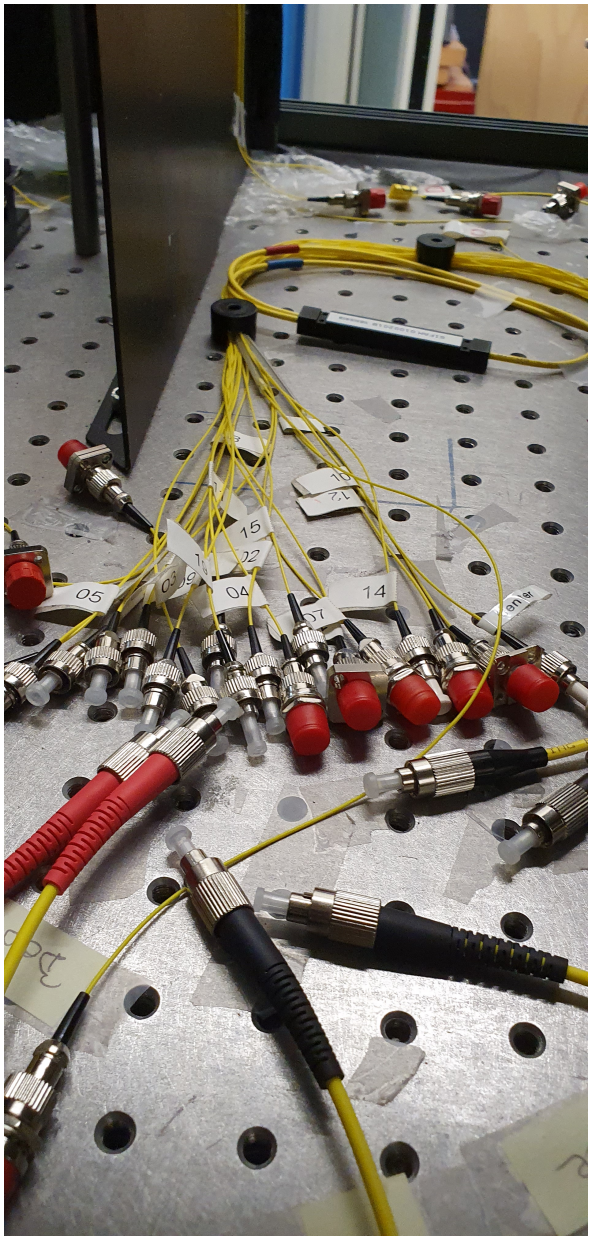

Fig. 10: SMFs attached on each core via a fan-in/fan-out device, allowing to use every core individually.

visibility above 94.8(3) % for all outer cores. Besides this, the polarization visibility was also measured to be above 81% for all cases (H/V and D/A basis for both rings) and therefore would suit quantum key distribution (QKD) schemes [49]. Further details and characteristics about the MCF can directly be taken from [49].

3.1.3 Interferometers

The spatial distribution of the entangled photons lead to an important effect on the MCF endface. As already discussed, an entangled pair enters the MCF in opposite cores, but is at the same time in a superposition of being in the adjacent cores. So this is the reason the photons are in the state described in Eq. 25. For this experiment four cores were taken in total - two opposite cores with an entangled pair (that we label A_1 and A_2) and again two opposite ones that are adjacent to the first pair (labeled B_1 and B_2), as depicted in Fig. 11. One core of each pair then guides to an interferometer, overlapping on a 50/50 BS. The fibres have a side-effect of rotating the polarization of the photons (each fibre does it differently) and those interfere only if they have identical polarization. By adding polarization controllers (PC) on each core and maximizing the power after a PBS ($|H\rangle$ photons are transmitted while $|V\rangle$ are reflected), it is ensured that only horizontally polarized photons are used for interference at the BS. Three single-mode couplers (where the photons are coupled into the interferometer) are placed on a translation-stage (two can be controlled with a computer software while the other is displaced by a micrometer screw) for alignment facilitation (see section 3.2). Now, one of those translation stages has an additional discrete piezoelectric stack mounted, which is used to periodically change the length of one arm, leading to a phase shift. After the BS the photons are coupled in again and are guided over SMFs to the detector. Both interferometers were built on a single damped breadboard.

3.1.4 Detector

The detector is a four channel superconducting nanowire single-photon detector[6] (SNSPD) with an efficiency of $\sim 80\,\%$ and a dark-count rate of $\sim 10^2$ Hz. A time-tagging module was used for further analysis and coincidences were determined by means of temporal cross-correlation functions. Integration time is set at 500 ms and a coincidence window of 300 ps. Since the efficiency of each channel is different and depends also on the polarization, PCs were used before detection to maximize counts.

3.2 Alignment procedure

First rough alignment was done using a telecom laser at a frequency of 1550 nm. The laser was coupled into both arms of the interferometer with a fibre-beamsplitter and the polarization was adjusted by measuring the power after the PBS and the use of the PCs. Laser viewing cards were placed right before the output couplers after the BS (or even further away using an additional mirror). Now, the beams were overlapped on the viewing card and almost perfect interference was achieved via beam walking. Afterwards, the beams were coupled into the SMFs that lead to the detector.
To ensure perfect interference, one could press against the breadboard (leading to a phase shift) and the beam area on the card should ideally go from very bright (perfect constructive

[6] Model: Single Quantum Eos

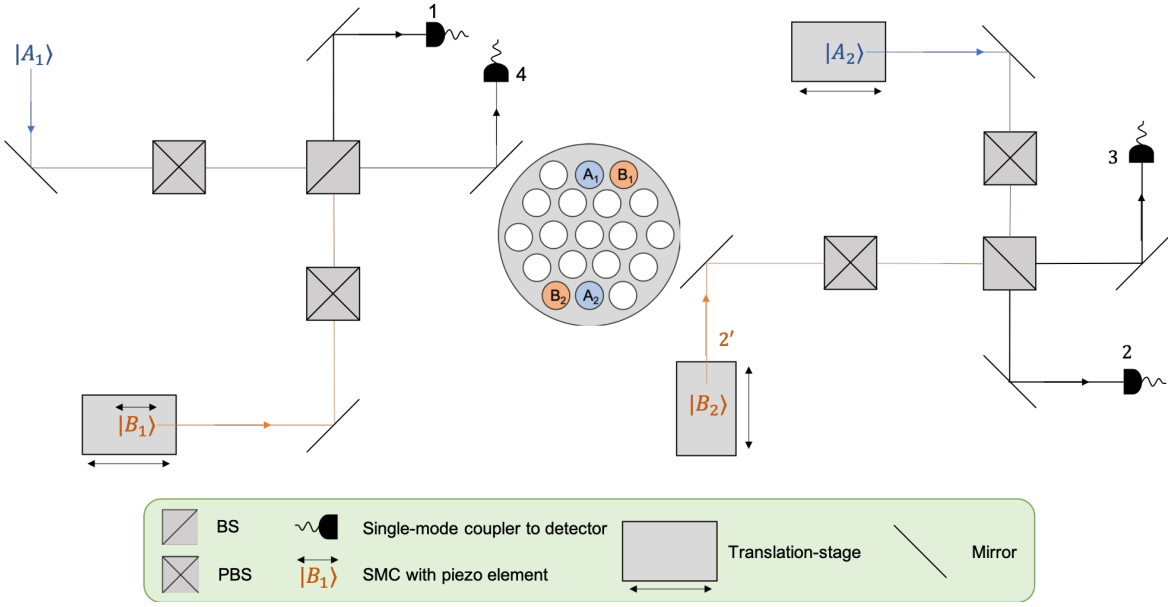

Fig. 11: Schematic interferometer setup. The cores A_1, B_1 and A_2, B_2 are entering the interferometers via SMFs and single mode couplers and overlap at the BS where the couplers after the BS lead them to the detector. A piezo element mounted on the translation-stage at the coupler of path B_1 will cause a phase shift. With the translation-stages alignment gets facilitated. In each path a PBS ensures only horizontally polarized photons. A photo of the setup is depicted in Fig. 12.

interference) to non-existent (perfect destructive interference). However, due to experimental imperfections a power-ratio between the maximum and the minimum of 50:1 is sufficient, where a ratio higher than 100:1 was always achieved. This was measured using a powermeter after the output coupler.
Next step involves switching from the laser to our entangled photons, which cannot be seen on the viewing card since the power is too small. For this, the SMFs of the cores get connected to the SMFs that are directly connected with the coupler of the interferometers. The previous alignment should not change and coincidences can be seen.
There are now four different paths in two interferometers that should all have the same length (from the origin of generation to the BS) up to a difference of the coherence length of the photons. To achieve this, the length of each arm was manually measured such that the couplers are driven with the translation-stages to the wanted position, which is only as good as the instrument that was used to determine the length allows[7]. If they had to be driven a lot then the alignment procedure had to be repeated, because the beams leaving the couplers are not parallel to the driving direction of the translation-stages. The last step includes using the coincidence peaks. Each (or some) photon traveling a different distance to the BS has an impact on the position of the peaks. One reference peak is chosen to be placed at $\tau = 0$ (here τ is a delay, not a time). Peaks now shifted to the right or left indicate a length difference in the arms, because the photons are arriving at a later or earlier time. Then the paths, for example, B_1 and B_2 get covered while driving the translation stage in A_2 until all peaks overlap at the center of zero delay. This was repeated with covering A_1 and A_2. To work properly, covering e.g. A_1 and B_1 and doing the same procedure should guarantee that all paths are

[7]The aimed length is the length of the arm that has no translation-stage, such that the remaining three can be repositioned.

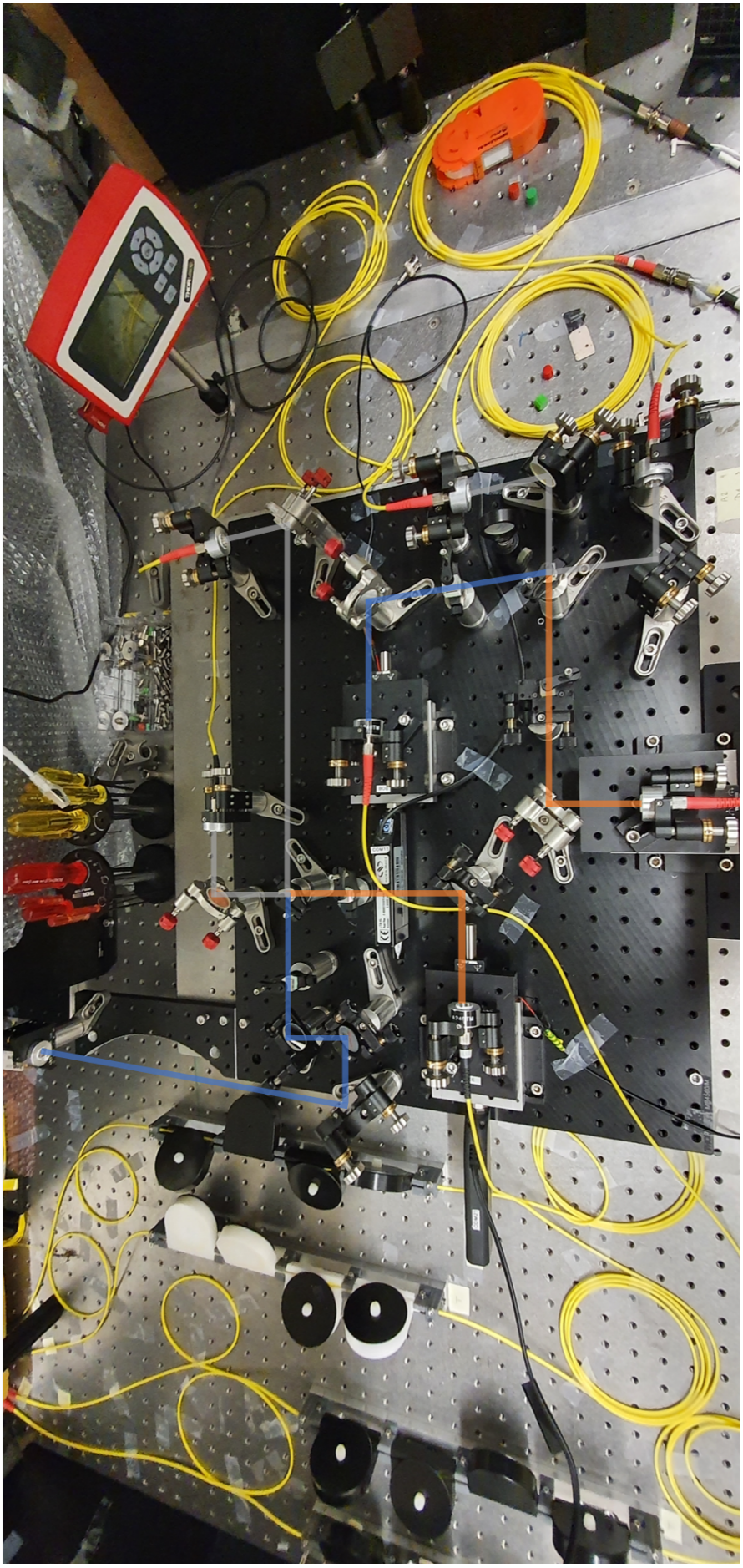

Fig. 12: Photo of the interferometers as sketched in Fig. 11. On the left hand side the PCs for each core can be seen.

of the same length, but A_1 and B_1 do not have cross-correlations, so coincidences cannot be seen. Therefore, it is to some extend a guessing game on which and how much the paths have to be adjusted. But this method worked very well and by simultaneous monitoring of the coincidence rates interference could be seen shortly after this adjustment.

3.2.1 Length difference of MCF cores

At first, the interferometers were aligned and coincidence peaks were monitored, every peak had a side-peak. After excluding effects like reflections within the interferometers or the fibre connectors, it was concluded that this second peak for every detector pairing must stem from a length difference of the MCF's cores. By putting an extra SMF between the core's SMF and the SMF of the coupler, additional shifting was observed. With that information convenient SMFs were added to the affected cores and the coupler's distance to the BS itself was adjusted to get rid of those side-peaks. Because 1 ns corresponds to 30 cm we knew how much length we had to add or take away. However, due to the higher refractive index in the fibre, the photons travel slower, with a speed of

$$c'(n) = \frac{c_0}{n} \tag{30}$$

where $c'(n)$ is the speed of light in a medium with refractive index n and c_0 is the vacuum speed limit. The fibres have a refractive index of $n = 1.515$ (BK7 glass). That's why when it looks like, for example, 30 cm had to be added, in reality it's roughly half of that length. But this length difference wasn't that easy to compensate, since SMFs only exist in discrete step-sizes. Therefore, additional fibres had to be combined with a displacement of the affected coupler - in our case it was coupler A_1 (see Fig. 11). An example of those side-peaks is shown in Fig. 13.

3.3 Stability

One point to mention is that even though the breadboard was not only on an optical table, but also stacked on an additional damping plate (on which the breadboard was mounted), the phase was periodically but irregularly changing. The reason is most probably thermal variations in the surrounding and between optical elements. Due to this effect the laser spot was transitioning between constructive and destructive interference during the alignment procedure. Hence, this interferometer under such circumstances is not stable and must eventually be considered for data analysis. In section 4.1 this will be discussed and concluded if, due to this fact, poissonian statistics is sufficient to describe photon uncertainties or different statistical analyzation methods have to be applied.

3.4 Measurement procedure

Because of the mechanical instability beside the typical measurement fluctuations, it was not possible to change the voltage on the piezo element at a stepwise, low constant rate. Instead, changing the voltage manually and continually, while monitoring the coincidence rate and as well as using a function generator[8] - connected to an amplifier[9] - that generates a linear ramp signal at low frequency has the same effect. With this procedure the magnitude

[8] Model: Agilent 33250A 80MHz Function/Arbitrary Waveform Generator
[9] Model: piezosystem jena ENT 400

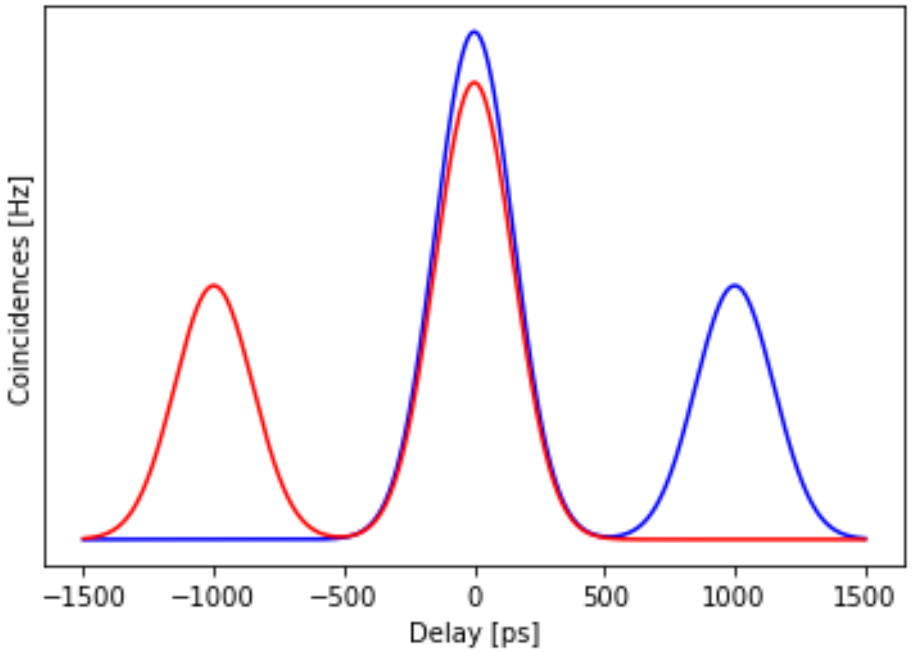

Fig. 13: Simulated coincidence peaks. This plot illustrates a histogram of the coincidences, which are calculated over the second order correlation function $g^{(2)}$. Each peak in the middle has a side-peak to the left or right (symmetric), indicating a length difference of around 1000 ps $\approx$ 30 cm in one arm. For demonstration, the coincidence peaks of only two detector-pairs are given. The other two pairs show the same behaviour.

of the fluctuations can be seen and a decision can be made on the spot if the measured phase curves are suitable for analysis or if more data is needed.

4 Results

During the monitoring of the coincidences the integration time was set at 500 ms while for the analysis (and therefore all following plots) a time of 1 s was chosen. Also, plots in which data points are connected (and without error bars) serve as a demonstration of the respective principle since with that amount of data, visibility curves or fluctuations would not be recognizable. Analyzed data is depicted correctly. The legend's notation is given by the detector-pairs, e.g. 13 are the coincidences between detector 1 and 3.

4.1 Data analysis

The aforementioned instability of the interferometers has two origins. First, the most dominant part, are the random phase-shifts caused by thermal variations in the environment between and around the optical elements. This variation can be seen in Fig. 14. In 500 s without changing the setup, one can see that the phase changes irregularly fast, rendering any measurement impossible.

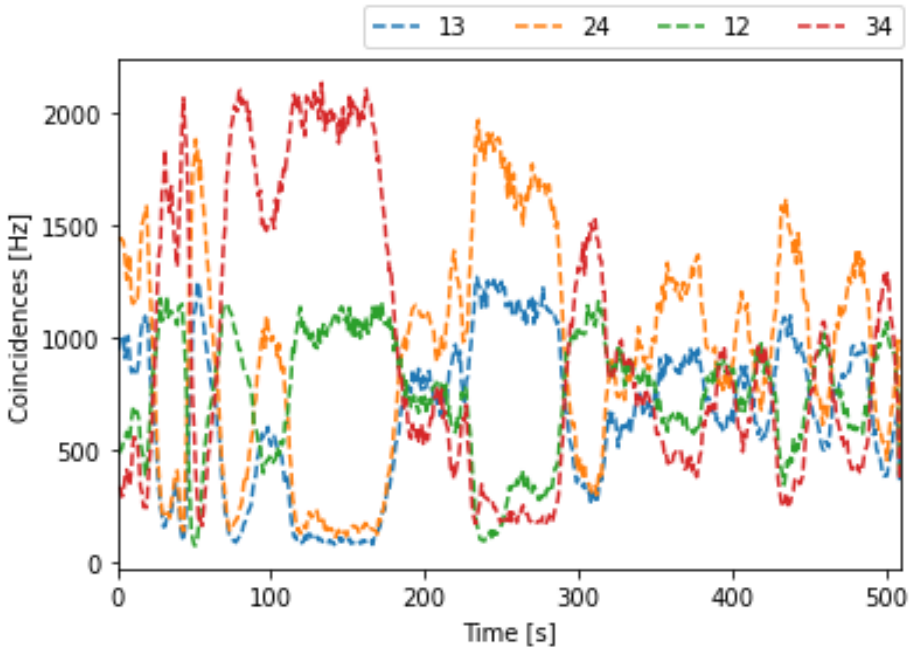

Fig. 14: A 500 s measurement without interacting with the setup. Phase-shifts occur unperiodically and randomly.

The second source has only an immaterial effect on the coincidence measurements. In one interferometer the single counts drop over time, while in the other they are more stable. Polarization drifts in the fibres are probably the reason for the losses - mostly in the fibres of the MCF. So after a certain time, the polarization had to be adjusted via the PCs. In Fig. 15 the single counts of each detector is depicted, where the loss in two channels is clearly visible. But as mentioned, they are not influencing the visibility but rather the heralding, so this can be neglected.
Fig. 14 is an extreme case of those fluctuations. Since the coincidence counts where monitored while measuring, it could be seen that the interferometers are sometimes stable enough and those fluctuations are not visible in the measurements. Hence, when the measurements where stable, the data can be used for analysis using poissonian statistics.

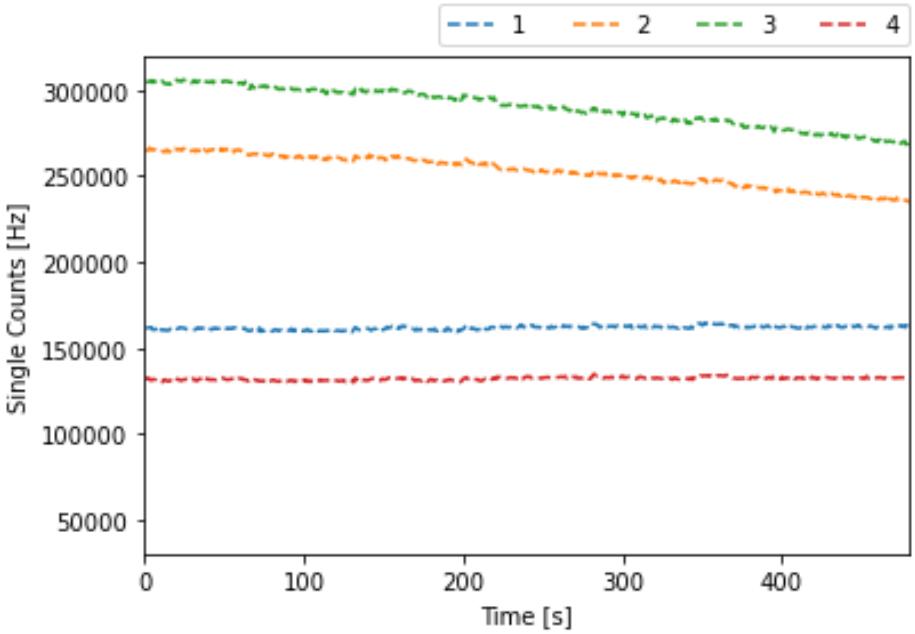

Fig. 15: Single counts of each detector channel for around 500 s. Due to polarization drifts in the fibres the two channels of one interferometer experience losses.

The dark-count rate for the four interesting detector-pairs can be seen in Fig. 16, where it can be observed that they do not exceed 17 counts per second. On average, each channel has following average accidentals $\bar{A}$ per second:

$$\bar{A}_{12} = 6 \qquad \bar{A}_{23} = 8$$
$$\bar{A}_{13} = 7 \qquad \bar{A}_{24} = 5$$
$$\bar{A}_{14} = 4 \qquad \bar{A}_{34} = 5$$

Those will be subtracted from their respective channels. As already discussed in chapter 2.3, two detector pairs do not show coincidences, namely 1 and 4 as well as 2 and 3. The measurements of those can be seen in Fig. 17. They will not be included in the plots for the visibility curves, since they are of no interest due to the almost zero coincidences.

4.2 Measurement

The measurements were done in two ways: Either by changing the voltage at the piezo element by hand continuously or using a function generator (ramp, 3 Hz), while simultaneously watching the coincidence rates. An example of a manually changed measurement can be viewed in Fig. 18. In this plot, the phase curves are clearly visible and fluctuations are not that large - in this case they probably stem from irregular modification of the voltage, since it is hard to change it by hand at an equal constant rate. Two measurements that were done using the function generator are depicted in Fig. 19. The left one shows a 90 s run, while the right one was measured for almost 500 s. The longer run shows some strong fluctuations in the range of 280 s – 400 s, which occurred when the voltage was manually changed, the ramp frequency got modified or the generator reached its maximum voltage output and regulated it back down (this happens faster than the ramp frequency). In both cases, the instability of the interferometers cannot be observed. So compared to the "by-hand

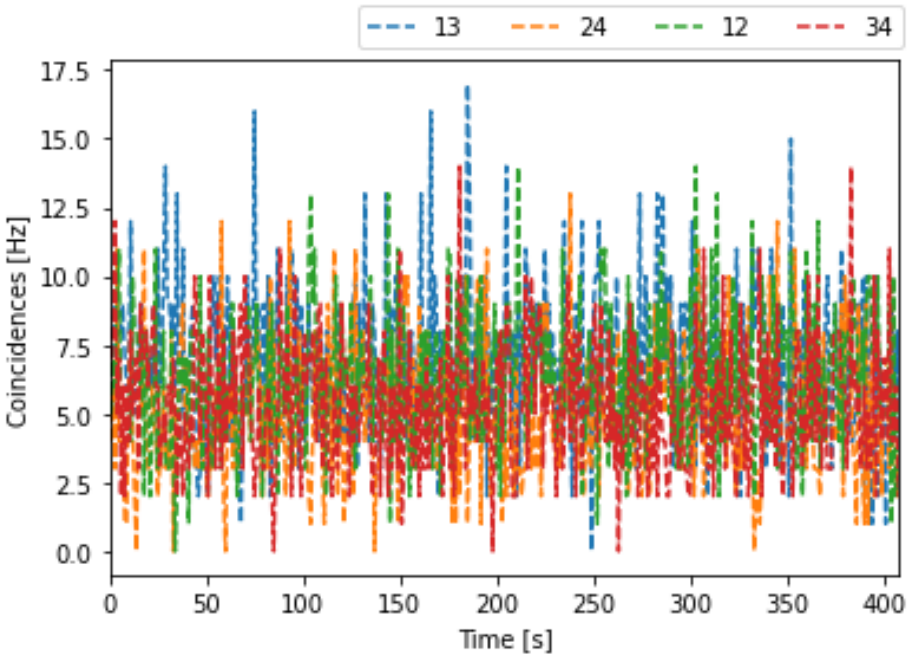

Fig. 16: Dark-counts for each detector-pair, except those with no correlations. For over 400 s they are not larger than 17 counts per second.

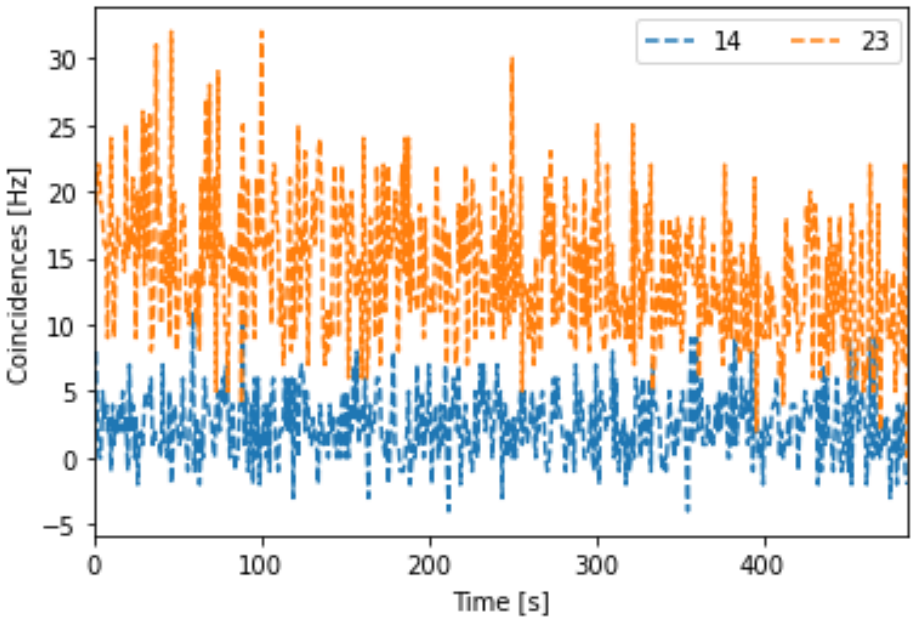

Fig. 17: Coincidence rate between detectors 2 and 3, as well as 1 and 4. The reason for the negative counts is the subtraction of the mean dark-count number. So channel 14 is almost at the zero level, while 23 is slightly above.

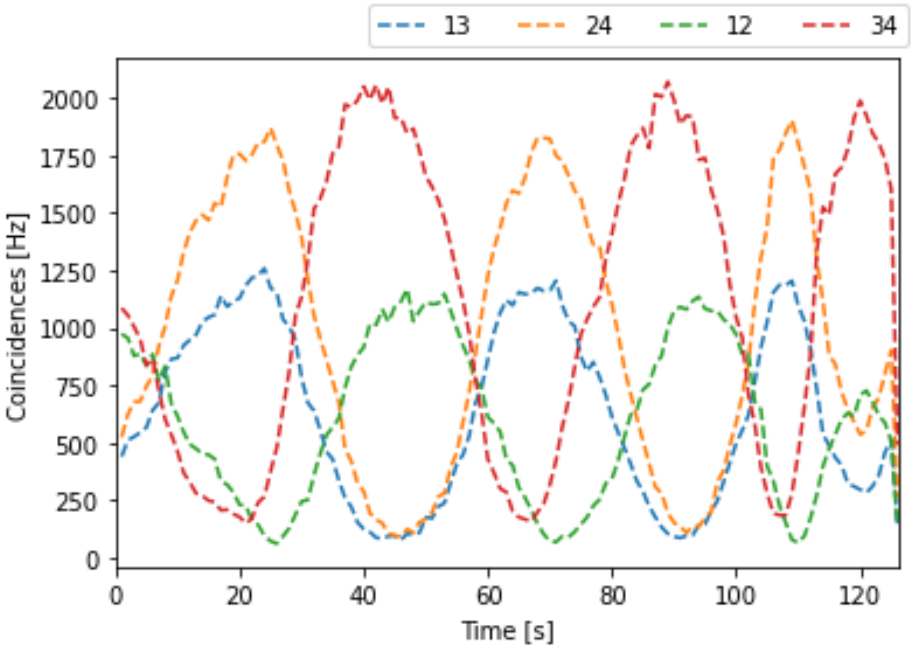

Fig. 18: 120 s measurement while changing the length of one arm by hand continuously and at an almost constant rate.

	Fig. 20	**Fig. 21**	**Fig. 22 (up)**	**Fig. 22 (down)**
V_{12}	0.859(51)	0.970(66)	0.970(62)	0.947(56)
V_{13}	0.897(54)	0.945(60)	0.937(51)	0.973(56)
V_{24}	0.912(44)	0.927(73)	0.923(59)	0.972(66)
V_{34}	0.852(38)	0.936(66)	0.945(61)	0.955(59)

Tab. 1: Computed visbilities from the plots with their respective uncertainties, calculated using gaussian error-propagation.

measurement" the function generator produces the best results. Also, the curves match the probabilities in Eq. (28).

4.3 Visibilities

In the following, we will analyze the visibilities of the conducted measurements. For that, three runs are taken for illustration. From those runs the data was fitted with a sine (squared) function inside a certain range, as we expect them to behave as given by Eq. (23). The visibilities are then calculated from this fit via Eq. (24), where C are now the coincidences. Fig. 20 illustrates the manually changed measurement run. The figure on the right shows the range marked on the left with the computed fit. Even in this case, a visibility between $85\,\% - 91\,\%$ was achieved, which is good enough for QKD applications.
For the measurements with the function generator, Fig. 21 shows the visibilites of one run, while Fig. 22 is the the same as Fig. 19 (right) but the end has been cut out. The visibilities for those generator assisted runs are all above 90 %, even reaching 97.2 %. In tab. 1 all visibilities incl. their uncertainties (computed using Gauss error-propagation) are listed regarding the shown plots.

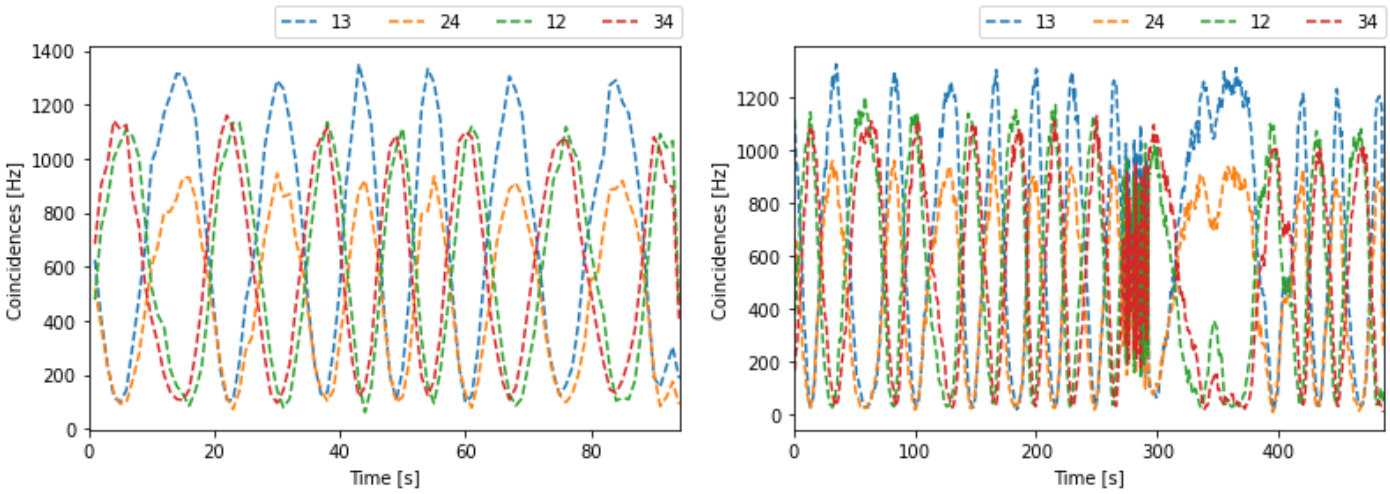

Fig. 19: (Left) 90s measurement using a function generator. (Right) 500s measurement - the inconsistency between 280s and 400s occurs when the voltage was manually changed, the ramp frequency got modified or the generator reached its maximum voltage output and regulates it back down (this happens faster than the ramp frequency)

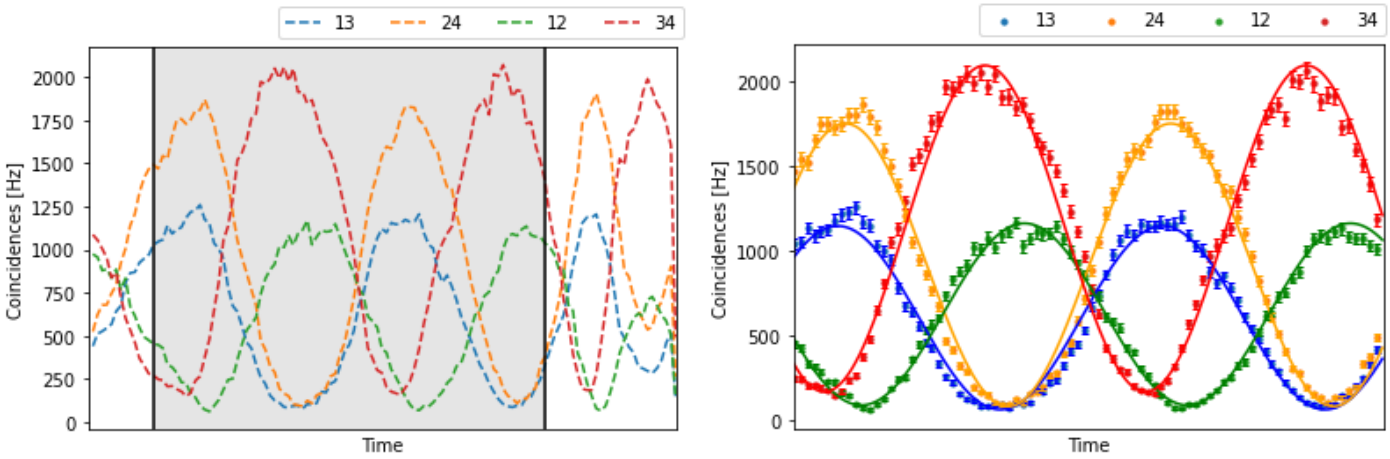

Fig. 20: (Left) 120s measurement while changing the length of one arm by hand and continuously. (Right) A fitted cut-out range. The visibilities are: $V_{13} = 0.897(54)$, $V_{12} = 0.859(51)$, $V_{24} = 0.912(44)$ and $V_{34} = 0.852(38)$.

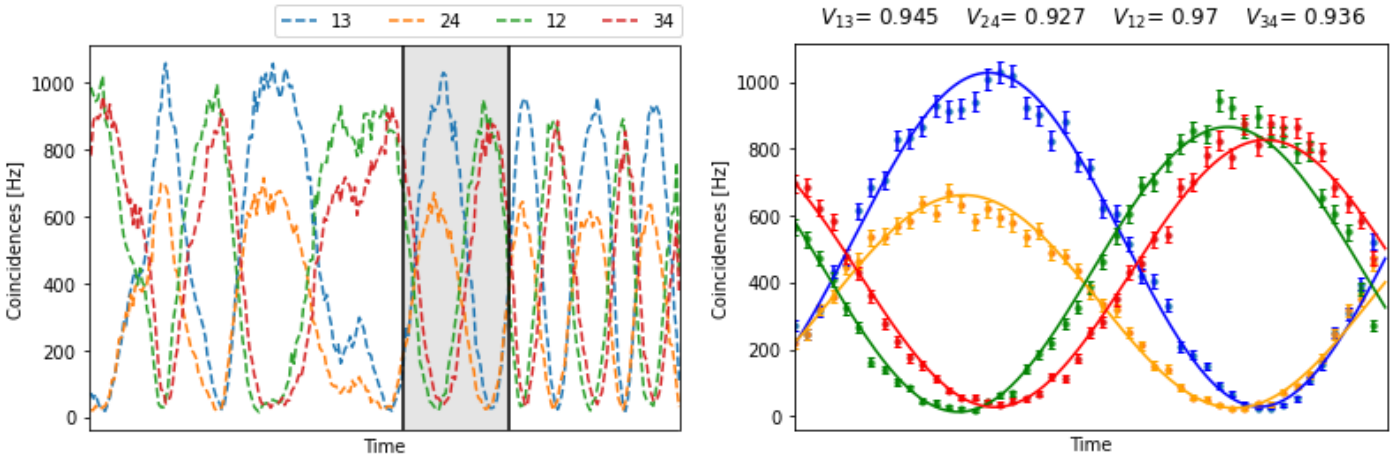

Fig. 21: (Left) Measurement with the function generator. The fluctuations before the marked range comes from changing settings on the generator. (Right) Visibility curve within the marked range. Visibilities can be seen atop of the figure - they are all above 90 %. Uncertainties are listed in tab. 1.

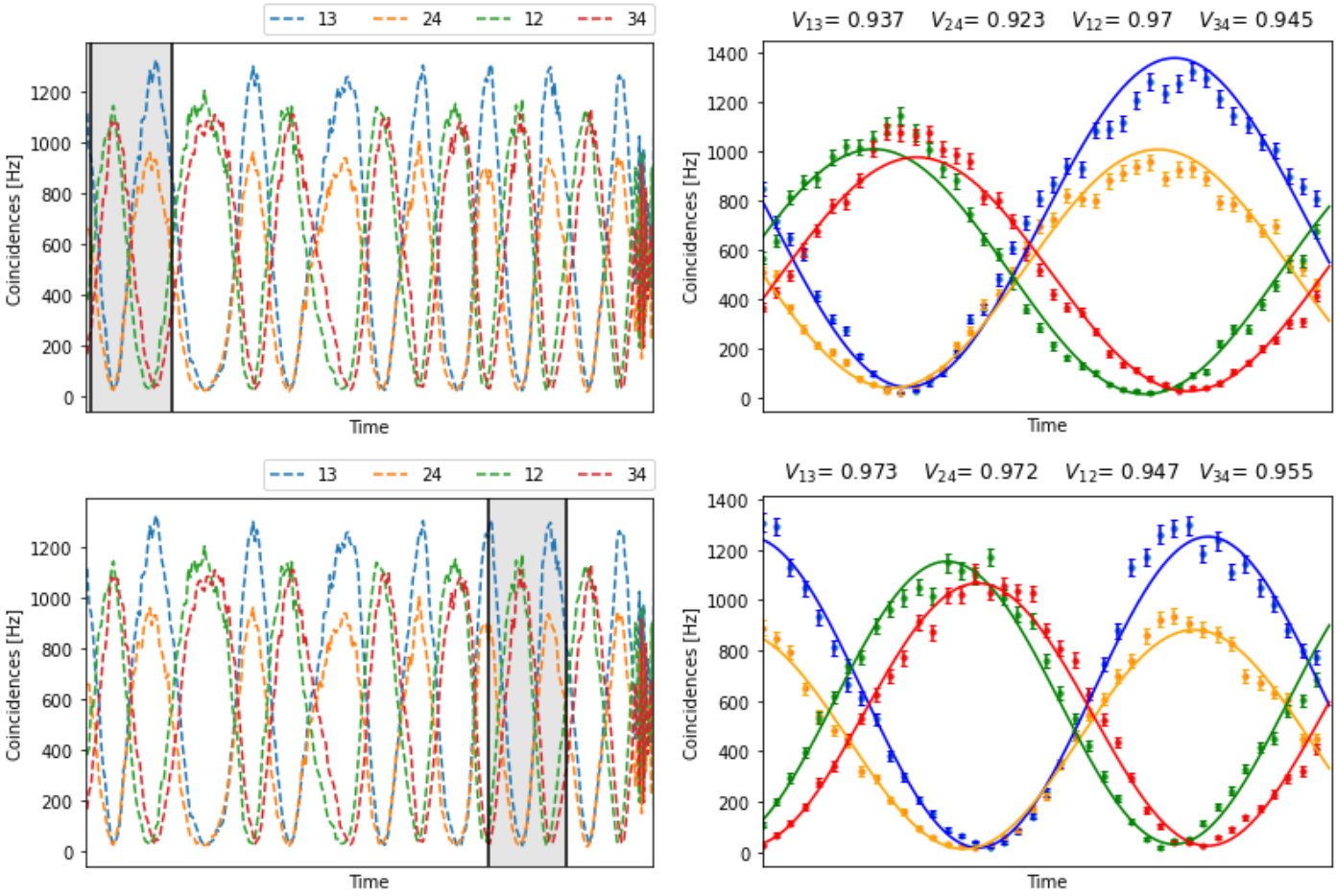

Fig. 22: (Left) This is the same run as in Fig. 19 (right) but before the large fluctuations. (Right) Again, the visibilites go way above 90 % even reaching 97 %. Uncertainties are listed in tab. 1.

5 Conclusion

Even though the setup was unstable and two different methods of measurements were used, the proof-of-principle of non-local interference via path entanglement could be shown, where a multicore fibre was used for transmission. By modifying the phase manually, a visibility of above 91 % was achieved. When using a function generator the visibility even reached 97 %. This result can be improved by fixing the stability issue - by a better isolation from the environment, getting rid of the polarization drifts inside the fibres or with laser stabilization. In each visibility plot a phase shift can be observed (maxima and minima are not aligned properly), a reason for that can be a small length difference in the interferometer arms. In this case the coincidence peaks could be covered from the main peak, making them impossible to see. Those still have to happen within the coherence length of the photons and therefore does not affect the visibilities. The visibility is basically a measure of how good the interference is. However, to see how good the entanglement itself is, one can calculate off-diagonal elements of the density matrix and compute the *fidelity*. This was done in further analysis of the data in [64]. There it was shown that the path visibility corresponds to an off-diagonal element of $\langle A_1 A_2|\rho|B_1 B_2\rangle = 0.24$ and hence a fidelity of $F_{\text{path}} = 0.953$. This experiment shows that a MCF is suitable for entanglement distribution by spatial multiplexing, enhancing the transmission capacity compared to a SMF. Due to the rotationally symmetric emission of the SPDC source, this method can be assumed to work for every other core pair, not only for these randomly selected cores. Operating this experiment with a wavelength of 1560 nm makes this method applicable for already existing telecommunication infrastructure. The same setup with an additional Franson interferometer was used to even show hyperentanglement in three degrees of freedom, but due to the limited detector channels only subsequently and not in parallel [64].

However, reaching such high visibilites also allows the usage of this principle for QKD applications, where the lower boundary for this employment lies at 81 %. Using this type of entanglement for QKD is currently starting to get researched. For example, using a MCF and changing the phase in one arm, one can alter the output paths of the entangled photons and therefore transmit them to other parties through the same channel. It has already been shown that path-entanglement as a part of hyperentangled states can lead to high key rates, even in very noisy environments [65]. New methods regarding path-entanglement and QKD will follow in the near future.

References

[1] R.L. Rivest, A. Shamir, and L. Adleman. A method for obtaining digital signatures and public-key cryptosystems. *Communications of the ACM*, 21:120–126, 1978.

[2] W. K. Wootters and W. H. Zurek. A single quantum cannot be cloned. *Nature*, 299(5886):802–803, October 1982.

[3] C. H. Bennett and G. Brassard. Quantum cryptography: Public key distribution and coin tossing. In *Proceedings of IEEE International Conference on Computers, Systems, and Signal Processing*, page 175, India, 1984.

[4] R. Ursin, F. Tiefenbacher, T. Schmitt-Manderbach, H. Weier, T. Scheidl, M. Lindenthal, B. Blauensteiner, T. Jennewein, J. Perdigues, P. Trojek, B. Ömer, M. Fürst, M. Meyenburg, J. Rarity, Z. Sodnik, C. Barbieri, H. Weinfurter, and A. Zeilinger. Entanglement-based quantum communication over 144km. *Nature Physics*, 3(7):481–486, July 2007.

[5] Fabian Steinlechner, Sebastian Ecker, Matthias Fink, Bo Liu, Jessica Bavaresco, Marcus Huber, Thomas Scheidl, and Rupert Ursin. Distribution of high-dimensional entanglement via an intra-city free-space link. *Nature Communications*, 8:15971, July 2017.

[6] Sören Wengerowsky, Siddarth Koduru Joshi, Fabian Steinlechner, Julien R. Zichi, Sergiy M. Dobrovolskiy, René van der Molen, Johannes W. N. Los, Val Zwiller, Marijn A. M. Versteegh, Alberto Mura, Davide Calonico, Massimo Inguscio, Hannes Hübel, Liu Bo, Thomas Scheidl, Anton Zeilinger, André Xuereb, and Rupert Ursin. Entanglement distribution over a 96-km-long submarine optical fiber. *Proceedings of the National Academy of Science*, 116(14):6684–6688, April 2019.

[7] Hui Liu, Cong Jiang, Hao-Tao Zhu, Mi Zou, Zong-Wen Yu, Xiao-Long Hu, Hai Xu, Shizhao Ma, Zhiyong Han, Jiu-Peng Chen, Yunqi Dai, Shi-Biao Tang, Weijun Zhang, Hao Li, Lixing You, Zhen Wang, Yong Hua, Hongkun Hu, Hongbo Zhang, Fei Zhou, Qiang Zhang, Xiang-Bin Wang, Teng-Yun Chen, and Jian-Wei Pan. Field Test of Twin-Field Quantum Key Distribution through Sending-or-Not-Sending over 428 km. *Physical Review Letters*, 126(25):250502, June 2021.

[8] Jiu-Peng Chen, Chi Zhang, Yang Liu, Cong Jiang, Wei-Jun Zhang, Zhi-Yong Han, Shi-Zhao Ma, Xiao-Long Hu, Yu-Huai Li, Hui Liu, Fei Zhou, Hai-Feng Jiang, Teng-Yun Chen, Hao Li, Li-Xing You, Zhen Wang, Xiang-Bin Wang, Qiang Zhang, and Jian-Wei Pan. Twin-field quantum key distribution over a 511 km optical fibre linking two distant metropolitan areas. *Nature Photonics*, 15(8):570–575, June 2021.

[9] Xiao-Min Hu, Cen-Xiao Huang, Yu-Bo Sheng, Lan Zhou, Bi-Heng Liu, Yu Guo, Chao Zhang, Wen-Bo Xing, Yun-Feng Huang, Chuan-Feng Li, and Guang-Can Guo. Long-Distance Entanglement Purification for Quantum Communication. *Physical Review Letters*, 126(1):010503, January 2021.

[10] Yu-Ao Chen, Qiang Zhang, Teng-Yun Chen, Wen-Qi Cai, Sheng-Kai Liao, Jun Zhang, Kai Chen, Juan Yin, Ji-Gang Ren, Zhu Chen, Sheng-Long Han, Qing Yu, Ken Liang, Fei Zhou, Xiao Yuan, Mei-Sheng Zhao, Tian-Yin Wang, Xiao Jiang, Liang Zhang, Wei-Yue Liu, Yang Li, Qi Shen, Yuan Cao, Chao-Yang Lu, Rong Shu, Jian-Yu Wang,

Li Li, Nai-Le Liu, Feihu Xu, Xiang-Bin Wang, Cheng-Zhi Peng, and Jian-Wei Pan. An integrated space-to-ground quantum communication network over 4,600 kilometres. *Nature*, 589(7841):214–219, January 2021.

[11] Leonard Susskind and Art Friedman. Quantum mechanics: The theoretical minimum. *Penguin Books*, 2015.

[12] Jianming Cai, Gian Giacomo Guerreschi, and Hans J. Briegel. Quantum Control and Entanglement in a Chemical Compass. *Physical Review Letters*, 104(22):220502, June 2010.

[13] Erik M. Gauger, Elisabeth Rieper, John J. L. Morton, Simon C. Benjamin, and Vlatko Vedral. Sustained Quantum Coherence and Entanglement in the Avian Compass. *Physical Review Letters*, 106(4):040503, January 2011.

[14] Beatrix C. Hiesmayr and Pawel Moskal. Genuine Multipartite Entanglement in the 3-Photon Decay of Positronium. *Scientific Reports*, 7:15349, November 2017.

[15] Dik Bouwmeester, Jian-Wei Pan, Klaus Mattle, Manfred Eibl, Harald Weinfurter, and Anton Zeilinger. Experimental quantum teleportation. *Nature*, 390(6660):575–579, December 1997.

[16] D. Bouwmeester, K. Mattle, J. W. Pan, H. Weinfurter, A. Zeilinger, and M. Zukowski. Experimental quantum teleportation of arbitrary quantum states. *Applied Physics B: Lasers and Optics*, 67(6):749–752, December 1998.

[17] Jian-Wei Pan, Dik Bouwmeester, Harald Weinfurter, and Anton Zeilinger. Experimental Entanglement Swapping: Entangling Photons That Never Interacted. *Physical Review Letters*, 80(18):3891–3894, May 1998.

[18] Thomas Jennewein, Gregor Weihs, Jian-Wei Pan, and Anton Zeilinger. Experimental Nonlocality Proof of Quantum Teleportation and Entanglement Swapping. *Physical Review Letters*, 88(1):017903, December 2001.

[19] Jian-Wei Pan, Sara Gasparoni, Rupert Ursin, Gregor Weihs, and Anton Zeilinger. Experimental entanglement purification of arbitrary unknown states. *Nature*, 423(6938):417–422, May 2003.

[20] Zhen Zhu Zhou, Wei He, Chun Dan Zhu, and Ying Wang. A Quantum Repeater Based on Entanglement Purification and Entanglement Swapping. *Applied Mechanics and Materials*, 302:607–611, February 2013.

[21] S. Parker, S. Bose, and M. B. Plenio. *Entanglement Purification via Entanglement Swapping*, pages 193–209. Springer Netherlands, Dordrecht, 2003.

[22] Reinhard F. Werner. Quantum states with Einstein-Podolsky-Rosen correlations admitting a hidden-variable model. *Physical Review A*, 40(8):4277–4281, October 1989.

[23] Asher Peres. Separability Criterion for Density Matrices. *Physical Review Letters*, 77(8):1413–1415, August 1996.

[24] Michał Horodecki, Paweł Horodecki, and Ryszard Horodecki. Separability of mixed states: necessary and sufficient conditions. *Physics Letters A*, 223(1):1–8, February 1996.

[25] Barbara M. Terhal. Bell inequalities and the separability criterion. *Physics Letters A*, 271(5-6):319–326, July 2000.

[26] Nicolai Friis, Giuseppe Vitagliano, Mehul Malik, and Marcus Huber. Entanglement certification from theory to experiment. *Nature Reviews Physics*, 1(1):72–87, January 2019.

[27] Stuart J. Freedman and John F. Clauser. Experimental Test of Local Hidden-Variable Theories. *Physical Review Letters*, 28(14):938–941, April 1972.

[28] B. Hensen, H. Bernien, A. E. Dréau, A. Reiserer, N. Kalb, M. S. Blok, J. Ruitenberg, R. F. L. Vermeulen, R. N. Schouten, C. Abellán, W. Amaya, V. Pruneri, M. W. Mitchell, M. Markham, D. J. Twitchen, D. Elkouss, S. Wehner, T. H. Taminiau, and R. Hanson. Loophole-free Bell inequality violation using electron spins separated by 1.3 kilometres. *Nature*, 526(7575):682–686, October 2015.

[29] Marissa Giustina, Marijn A. M. Versteegh, Sören Wengerowsky, Johannes Handsteiner, Armin Hochrainer, Kevin Phelan, Fabian Steinlechner, Johannes Kofler, Jan-Åke Larsson, Carlos Abellán, Waldimar Amaya, Valerio Pruneri, Morgan W. Mitchell, Jörn Beyer, Thomas Gerrits, Adriana E. Lita, Lynden K. Shalm, Sae Woo Nam, Thomas Scheidl, Rupert Ursin, Bernhard Wittmann, and Anton Zeilinger. Significant-Loophole-Free Test of Bell's Theorem with Entangled Photons. *Physical Rreview Letters*, 115(25):250401, December 2015.

[30] I. Marcikic, H. de Riedmatten, W. Tittel, V. Scarani, H. Zbinden, and N. Gisin. Time-bin entangled qubits for quantum communication created by femtosecond pulses. *Physical Review A*, 66(6):062308, December 2002.

[31] I. Marcikic, H. de Riedmatten, W. Tittel, H. Zbinden, M. Legré, and N. Gisin. Distribution of Time-Bin Entangled Qubits over 50km of Optical Fiber. *Physical Revieq Letters*, 93(18):180502, October 2004.

[32] Itai Afek, Oron Ambar, and Yaron Silberberg. High-NOON States by Mixing Quantum and Classical Light. *Science*, 328(5980):879, May 2010.

[33] Y. Israel, I. Afek, S. Rosen, O. Ambar, and Y. Silberberg. Experimental tomography of NOON states with large photon numbers. *Physical Review A*, 85(2):022115, February 2012.

[34] Philip Walther, Jian-Wei Pan, Markus Aspelmeyer, Rupert Ursin, Sara Gasparoni, and Anton Zeilinger. De Broglie wavelength of a non-local four-photon state. *Nature*, 429(6988):158–161, May 2004.

[35] Francesco Graffitti, Vincenzo D'Ambrosio, Massimiliano Proietti, Joseph Ho, Bruno Piccirillo, Corrado de Lisio, Lorenzo Marrucci, and Alessandro Fedrizzi. Hyperentanglement in structured quantum light. *Physical Review Research*, 2(4):043350, December 2020.

[36] Meiyu Wang, Fengli Yan, and Ting Gao. Entanglement purification of two-photon systems in multiple degrees of freedom. *Quantum Information Processing*, 19(7):206, June 2020.

[37] Cheng-Yan Gao, Bao-Cang Ren, Yuan-Xia Zhang, Qing Ai, and Fu-Guo Deng. Universal linear-optical hyperentangled Bell-state measurement. *Applied Physics Express*, 13(2):027004, February 2020.

[38] David C. Burnham and Donald L. Weinberg. Observation of Simultaneity in Parametric Production of Optical Photon Pairs. *Physical Review Letters*, 25(2):84–87, July 1970.

[39] O. Gayer, Z. Sacks, E. Galun, and A. Arie. Temperature and wavelength dependent refractive index equations for MgO-doped congruent and stoichiometric $LiNbO_3$. *Applied Physics B: Lasers and Optics*, 91(2):343–348, May 2008.

[40] M.M. Fejer, G.A. Magel, D.H. Jundt, and R.L. Byer. Quasi-phase-matched second harmonic generation: tuning and tolerances. *IEEE Journal of Quantum Electronics*, 28(11):2631–2654, 1992.

[41] X. P. Hu, P. Xu, and S. N. Zhu. Engineered quasi-phase-matching for laser techniques [invited]. *Photon. Res.*, 1(4):171–185, Dec 2013.

[42] P. Xu and S. N. Zhu. Review Article: Quasi-phase-matching engineering of entangled photons. *AIP Advances*, 2(4):041401, December 2012.

[43] S. P. Walborn, C. H. Monken, S. Pádua, and P. H. Souto Ribeiro. Spatial correlations in parametric down-conversion. *Physics Reports*, 495(4-5):87–139, October 2010.

[44] Evelyn A. Ortega, Jorge Fuenzalida, Mirela Selimovic, Krishna Dovzhik, Lukas Achatz, Sören Wengerowsky, Rodrigo F. Shiozaki, Sebastian P. Neumann, Martin Bohmann, and Rupert Ursin. Spatial and spectral characterization of telecommunication-wavelength photon pairs created in a type-0 mgo:ppln crystal. In preparation.

[45] Sebastian Philipp Neumann. Towards narrow-band photon pair sources for continuous-wave entanglement swapping. Master's thesis, University of Vienna, 2015.

[46] A. Zeilinger. General properties of lossless beam splitters in interferometry. *American Journal of Physics*, 49(9):882–883, September 1981.

[47] Evelyn A. Ortega, Krishna Dovzhik, Jorge Fuenzalida, Sören Wengerowsky, Juan Carlos Alvarado-Zacarias, Rodrigo F. Shiozaki, Rodrigo Amezcua-Correa, Martin Bohmann, and Rupert Ursin. Experimental space-division multiplexed polarization-entanglement distribution through 12 paths of a multicore fiber. *PRX Quantum*, 2:040356, Dec 2021.

[48] Taehyun Kim, Marco Fiorentino, and Franco N. C. Wong. Phase-stable source of polarization-entangled photons using a polarization sagnac interferometer. *Phys. Rev. A*, 73:012316, Jan 2006.

[49] Evelyn A. Ortega, Krishna Dovzhik, Jorge Fuenzalida, Sören Wengerowsky, Juan Carlos Alvarado-Zacarias, Rodrigo F. Shiozaki, Rodrigo Amezcua-Correa, Martin Bohmann, and Rupert Ursin. Experimental Space-Division Multiplexed Polarization-Entanglement Distribution through 12 Paths of a Multicore Fiber. *PRX Quantum*, 2(4):040356, December 2021.

[50] Juan Yin, Ji-Gang Ren, He Lu, Yuan Cao, Hai-Lin Yong, Yu-Ping Wu, Chang Liu, Sheng-Kai Liao, Fei Zhou, Yan Jiang, Xin-Dong Cai, Ping Xu, Ge-Sheng Pan, Jian-Jun Jia, Yong-Mei Huang, Hao Yin, Jian-Yu Wang, Yu-Ao Chen, Cheng-Zhi Peng, and Jian-Wei Pan. Quantum teleportation and entanglement distribution over 100-kilometre free-space channels. *Nature*, 488(7410):185–188, August 2012.

[51] Sheng-Kai Liao, Wen-Qi Cai, Johannes Handsteiner, Bo Liu, Juan Yin, Liang Zhang, Dominik Rauch, Matthias Fink, Ji-Gang Ren, Wei-Yue Liu, Yang Li, Qi Shen, Yuan Cao, Feng-Zhi Li, Jian-Feng Wang, Yong-Mei Huang, Lei Deng, Tao Xi, Lu Ma, Tai Hu, Li Li, Nai-Le Liu, Franz Koidl, Peiyuan Wang, Yu-Ao Chen, Xiang-Bin Wang, Michael Steindorfer, Georg Kirchner, Chao-Yang Lu, Rong Shu, Rupert Ursin, Thomas Scheidl, Cheng-Zhi Peng, Jian-Yu Wang, Anton Zeilinger, and Jian-Wei Pan. Satellite-Relayed Intercontinental Quantum Network. *Physical Review Letters*, 120(3):030501, January 2018.

[52] Liu-Jun Wang, Luo-Kan Chen, Lei Ju, Mu-Lan Xu, Yong Zhao, Kai Chen, Zeng-Bing Chen, Teng-Yun Chen, and Jian-Wei Pan. Experimental multiplexing of quantum key distribution with classical optical communication. *Applied Physics Letters*, 106(8):081108, February 2015.

[53] J. Chen, G. Wu, L. Xu, X. Gu, E. Wu, and H. Zeng. Stable quantum key distribution with active polarization control based on time-division multiplexing. *New Journal of Physics*, 11(6):065004, June 2009.

[54] Sören Wengerowsky, Siddarth Koduru Joshi, Fabian Steinlechner, Hannes Hübel, and Rupert Ursin. An entanglement-based wavelength-multiplexed quantum communication network. *Nature*, 564(7735):225–228, December 2018.

[55] Zhi-Yu Chen, Lian-Shan Yan, Yan Pan, Lin Jiang, An-Lin Yi, Wei Pan, and Bin Luo. Use of polarization freedom beyond polarization-division multiplexing to support high-speed and spectral-efficient data transmission. *Light: Science & Applications*, 6(2):e16207–e16207, February 2017.

[56] D. J. Richardson, J. M. Fini, and L. E. Nelson. Space-division multiplexing in optical fibres. *Nature Photonics*, 7(5):354–362, May 2013.

[57] Liang Cui, Jie Su, Xiaoying Li, and Z. Y. Ou. Distribution of entangled photon pairs over few-mode fibers. *Scientific Reports*, 7:14954, November 2017.

[58] W. Löffler, T. G. Euser, E. R. Eliel, M. Scharrer, P. St. J. Russell, and J. P. Woerdman. Fiber Transport of Spatially Entangled Photons. *Physical Review Letters*, 106(24):240505, June 2011.

[59] Saroch Leedumrongwatthanakun, Luca Innocenti, Hugo Defienne, Thomas Juffmann, Alessandro Ferraro, Mauro Paternostro, and Sylvain Gigan. Programmable linear quantum networks with a multimode fibre. *Nature Photonics*, 14(3):139–142, December 2019.

[60] G. Cañas, N. Vera, J. Cariñe, P. González, J. Cardenas, P. W. R. Connolly, A. Przysiezna, E. S. Gómez, M. Figueroa, G. Vallone, P. Villoresi, T. Ferreira da Silva, G. B. Xavier, and G. Lima. High-dimensional decoy-state quantum key distribution over multicore telecommunication fibers. *Physical Review A*, 96(2):022317, August 2017.

[61] Yunhong Ding, Davide Bacco, Kjeld Dalgaard, Xinlun Cai, Xiaoqi Zhou, Karsten Rottwitt, and Leif Katsuo Oxenløwe. High-dimensional quantum key distribution based on multicore fiber using silicon photonic integrated circuits. *npj Quantum Information*, 3:25, June 2017.

[62] Hee Jung Lee, Sang-Kyung Choi, and Hee Su Park. Experimental Demonstration of Four-Dimensional Photonic Spatial Entanglement between Multi-core Optical Fibres. *Scientific Reports*, 7:4302, June 2017.

[63] E. S. Gómez, S. Gómez, I. Machuca, A. Cabello, S. Pádua, S. P. Walborn, and G. Lima. Multidimensional Entanglement Generation with Multicore Optical Fibers. *Physical Review Applied*, 15(3):034024, March 2021.

[64] Lukas Achatz, Lukas Bulla, Evelyn A. Ortega, Michael Bartokos, Sebastian Ecker, Martin Bohmann, Rupert Ursin, and Marcus Huber. Simultaneous transmission of hyper-entanglement in 3 degrees of freedom through a multicore fiber. `arXiv:2208.10777 [quant-ph]`, 2022.

[65] Xiao-Min Hu, Chao Zhang, Yu Guo, Fang-Xiang Wang, Wen-Bo Xing, Cen-Xiao Huang, Bi-Heng Liu, Yun-Feng Huang, Chuan-Feng Li, Guang-Can Guo, Xiaoqin Gao, Matej Pivoluska, and Marcus Huber. Pathways for Entanglement-Based Quantum Communication in the Face of High Noise. *Physical Review Letters*, 127(11):110505, September 2021.